

A FIRST-PRINCIPLES STUDY ON BULK CuO:
ELECTRONIC STRUCTURES AND
NATIVE POINT DEFECTS

by

DANGXIN WU

Presented to the Faculty of the Graduate School of
The University of Texas at Arlington in Partial Fulfillment
of the Requirements
for the Degree of

MASTER OF SCIENCE IN PHYSICS

THE UNIVERSITY OF TEXAS AT ARLINGTON

AUGUST 2005

Copyright © by Dangxin Wu 2005

All Rights Reserved

ACKNOWLEDGEMENTS

It is my pleasure to have this opportunity to thank many people who have helped me in various ways and whose support has been invaluable over the past two and half years. Firstly, I must say I have been very fortunate to have a supervisor of the caliber of Dr. Qiming Zhang. I am very grateful for his scientific guidance and patient supervision. His constant support, wisdom and encouragement have kept me going over the last two and half years and this project. I would also like to thank Dr. John L. Fry, Dr. Asok K. Ray and Dr. Meng Tao for serving in my thesis committee and for helping me in many other aspects.

I am indebted to my colleagues and friends both in this department and in China. There is no sufficient space to list all of them. But I value their encouragements, discussions and sharing in my study, my research and my life. Thanks also to the faculty and staff of the Physics Department. The kind help and support from them have made my life in UTA joyful and unforgettable.

And my long due thanks should be given to my family, especially my wife Jinli Li, for their love, support and belief in my abilities, without which I would never have got here.

This work is partly supported by Texas Advanced Technology Program (ATP).

July 22, 2005

ABSTRACT

A FIRST-PRINCIPLES STUDY ON BULK CuO: ELECTRONIC STRUCTURES AND NATIVE POINT DEFECTS

Publication No. _____

Dangxin Wu, M.S.

The University of Texas at Arlington, 2005

Supervising Professor: Qiming Zhang

In this thesis, we have performed a first-principles study on strongly correlated monoclinic cupric oxide (CuO) by using the LSDA+U method implemented in the PAW method. Based on the optimized structural parameters, which are in good agreement with the experimental data, the electronic structure and the magnetic properties are obtained. Our calculations show that CuO is a semiconducting material with an indirect gap of about 1.0 eV. The semiconducting nature of CuO from our calculations is consistent with many experiments, but is qualitatively different from the LSDA calculations which incorrectly predict CuO to be metallic. The indirect gap of 1.0 eV is also in good agreement with many experimental results. We also found that in

its ground state, CuO is antiferromagnetic with a local magnetic moment per formula of about $0.60 \mu_B$, which is close to the experimental values.

By applying the LSDA+U method to a $2 \times 3 \times 2$ supercell using the optimized structural parameters, we examine the structural relaxations, defect levels and defect formation energies of some possible native point defect in CuO. The results of the formation energies of the native point defects show that both in Cu-rich and O-rich environments, negatively charged Cu vacancies can be more easily formed in CuO than other native point defects. This explains why CuO is intrinsically a p-type semiconductor as measured by several experiments.

TABLE OF CONTENTS

ACKNOWLEDGEMENTS.....	iii
ABSTRACT	iv
LIST OF ILLUSTRATIONS.....	viii
LIST OF TABLES.....	xi
 Chapter	
1. INTRODUCTION.....	1
2. METHODOLOGY.....	6
2.1 Schrödinger Equation	6
2.2 The Born-Oppenheimer Approximation.....	8
2.3 Density Functional Theory	10
2.3.1 The Hohenberg-Kohn Theorems	11
2.3.2 The Kohn-Sham Method	15
2.3.3 Spin Density Functional Theory.....	19
2.4 Approximations of $E_{xc}[\rho]$: L(S)DA and GGA	20
2.5 Strongly Correlated Systems and LSDA+U Method.....	23
2.6 Solving the Kohn-Sham Equations.....	25
2.6.1 Bloch's Theorem and \mathbf{k} Point Sampling	26
2.6.2 Plane Wave Basis Sets and Pseudopotential Approximation.....	28

2.6.3 The Projector Augmented Wave (PAW) Method	29
2.6.4 Implementation of LSDA+U within PAW Method.....	32
2.6.5 The Self-Consistent Procedure	33
3. STRUCTURAL, ELECTRONIC AND MAGNETIC PROPERTIES OF CRYSTAL CuO	35
3.1 Computational Details	35
3.2 Crystal Structure.....	36
3.3 Electronic Structure	38
3.4 Magnetic Properties	45
3.5 Discussion.....	47
4. NATIVE POINT DEFECTS IN BULK CuO	48
4.1 Computational Details	48
4.1.1 Supercell Geometry	48
4.1.2 Calculating Formation Energies	51
4.2 Results and Discussions.....	52
4.2.1 Electronic Structures and Structural Relaxations	53
4.2.2 Formation Energies.....	57
5. CONCLUSION AND FURTHER WORK	60
REFERENCES	62
BIOGRAPHICAL INFORMATION.....	71

LIST OF ILLUSTRATIONS

Figure	Page
<p>2.1 Schematic representation of Hohenberg-Kohn theorems. The single arrows denote the usual solution of the Schrödinger equation where the potential $V_{ext}(r)$ determines all states of the system $\psi_i(r)$, including the ground state $\psi_0(r)$ and ground density $n_0(r)$. The double arrow labeled “HK” denotes the Hohenberg-Kohn theorems, which completes the cycle.....</p>	11
<p>2.2 A cartoon representing the relationship between the real many body system (left hand side) and the auxiliary non-interacting system of Kohn-Sham method.....</p>	15
<p>2.3 Schematic representation of Kohn-Sham method. The notation HK_0 denotes the Hohenberg-Kohn theorems applied to the non-interacting problem. The arrow labeled KS provides the connection in both directions between the many-body and single-particle systems. Therefore, in principle, solution of the single-particle Kohn-Sham problem determines all properties of the many-body system.</p>	19
<p>2.4 Schematic representation of the self-consistent loop to solve the Kohn-Sham equations</p>	34
<p>3.1 The crystal structure of cupric oxide. Black circles indicate O atoms, while grey circles indicate Cu atoms. (a) Side view. (b) Top view along the b axis.....</p>	37
<p>3.2 Density of states calculated using the LSDA method. The Fermi level is set at 0 eV. The majority is plotted upward; the minority is plotted downward.....</p>	39

3.3	Density of states calculated using the LSDA+U method for CuO. The Fermi level is set at 0 eV. The majority is plotted upward; the minority is plotted downward. The symmetric filling of both majority and minority electrons indicates an antiferromagnetic ground state.....	40
3.4	The first Brillouin zone of monoclinic structure.....	41
3.5	Band structure of CuO calculated using the LSDA method. The Fermi level is set at 0 eV.....	43
3.6	Band structure of CuO calculated using the LSDA+U method. The Fermi level is set at 0 eV.....	44
3.7	The unit cell of CuO with spin alignments corresponding to the lowest total energy. For the same lowest energy, the spin alignments could be totally reversed. Black circles indicate O atoms, while grey circles indicate Cu atoms. The atoms are numbered for the convenience of differentiating in Table 3.2 later.....	45
4.1	Structure of CuO supercell containing 96 atoms used in the study in this section. Black circles indicate O atoms, while grey circles indicate Cu atoms	50
4.2	Initial interstitial position considered in the unit cell of CuO. Black circles indicate O atoms, while grey circles indicate Cu atoms. The interstitial is represented by a light grey circle.....	52
4.3	Densities of states (DOS) for perfect CuO supercell and defective supercells. The valence band maxima are set at 0 eV. The majority is plotted upward; the minority is plotted downward. (a) Perfect, (b) Cu_O^0 , (c) O_Cu^0 , (d) V_Cu^0 , (e) V_O^0 , (f) Cu_i^0 , and (g) V_i^0	56
4.4	Formation energies of native point defects in CuO as a function of the Fermi level E_F in the O-rich environment. For each defect species, only the lowest-energy charge states with respect to E_F are shown. The zero energy of E_F corresponds to the valance band maximum.....	58

4.5 Formation energies of native point defects in CuO as a function of the Fermi level E_F in the Cu-rich environment. For each defect species, only the lowest-energy charge states with respect to E_F are shown. The zero energy of E_F corresponds to the valance band maximum. 58

LIST OF TABLES

Table	Page
3.1 Calculated structural parameters for unit cell of CuO and their comparisons with experimental results. β is the angle between lattice vectors a and c in the monoclinic cell and u is a parameter describing the relative positions of O atoms along lattice vector b	38
3.2 Decomposed magnetic moments in μ_B of atoms in the unit cell of CuO. The numbers of ions are assigned as shown in Figure 3.7	46
4.1 Structural relaxations around native point defects. Average distances from the defect positions to neighboring ions are listed. Neighboring atomic species and their coordination number are also shown in parentheses	54

CHAPTER 1

INTRODUCTION

It is reported that the remaining stocks of recoverable fossils are optimistically estimated to last less than 170 years [1]. However, global energy consumption and projected demand are rising considerably, implying an energy shortage in the near future. In addition, the emissions of oxides of carbon and sulfur resulting from burning fossil fuels for energy generation are increasingly endanger the ecological stability of the earth, causing acid rain and the greenhouse effect, and also leading to many health problems for human beings. To solve these problems, we have to explore alternatives of fossil fuels for energy generation. One of the most attractive alternatives is solar energy because it is one of the biggest energy resources and most homogeneously spread over the globe. In one hour, the Earth receives enough energy from the sun to meet its energy needs for nearly a year [2]. As one of the most important long-term technologies for using solar energy, photovoltaic (PV) cells or solar cells as they are often referred to, utilize the photovoltaic effects as an energy conversion process and have many advantages including [3]: they are environmentally benign; they are reliable and require little maintenance; they can be integrated into buildings and other constructions.

There are already some PV cells in production and in use. But the shortcomings with these currently used PV cells have limited their uses extensively. For instance, silicon (Si) cells and Gallium Arsenide (GaAs) cells have high production cost due to the need of clean rooms; Copper Indium Diselenide (CIS) cells use indium, which is rare, and selenium, which is somewhat rare; Cadmium Telluride (CdTe) cells use heavy metal Cd, which is rare and has adverse environmental impacts.

However, many semiconducting metal oxides (SMOs) can avoid these problems. Their constituent metallic elements are rich in the Earth and not harmful to the environment. Most importantly, they can be fabricated through wet chemical process and therefore have low production cost. Taking into account of the solar spectrum characteristics and optimal efficiency of the cells (defined as the ratio of the maximum electrical power output to the solar power arriving on unit area), an ideal semiconductor for PV cells should have a band gap E_g at 1.4-1.5 eV. For this reason, many SMOs, such as TiO_2 and ZnO ($E_g > 3$ eV) cannot be directly used as materials for PV cells. But cupric oxide (CuO), as one of SMOs, with a reported experimental band gap of 1.2-1.9 eV [4-8], seems an attractive material in this respect. Indeed, in the past few years, CuO has attracted increasing interest as promising materials for PV cells due to its suitable optical properties. It can absorb sun light throughout the visible region with the reported band gap. Besides, the natural abundance of its constituents, the low fabrication cost, its stability and non-toxic nature, and its reasonably good electrical properties have made it a promising candidate material for large-area low-cost PV systems.

Due to its fundamental importance in understanding some high-temperature superconductors [8-10] and its potential usage in PV cells and other practical applications such as gas sensors [11], magnetic storage media [12], electronics [13], semiconductors [14], varistors [15] and catalysis [16], CuO has been investigated extensively in the experimental aspect. X-ray diffraction [17] shows that the crystal structure of CuO is monoclinic with $C2/c$ symmetry and with four formula units per unit cell. It has a semiconducting ground state and is found as p-type in many experiments [8, 18-20]. The magnetic properties have been studied by neutron scattering experiments and it is found that CuO is antiferromagnetic below 220 K with the local magnetic moment per unit formula about $0.65 \mu_B$ [21-25]. On the other hand, only a few theoretical studies have been done on this material with limited and somehow incorrect results, probably because of its complicated crystal structure but most importantly, its strong-correlated electronic nature. The electronic structure of CuO has been studied using cluster model calculations [26] and *ab initio* calculations based on the local spin density approximation (LSDA) [27-29]. But these calculations failed to predict the semiconducting ground state. Instead, they predicted a nonmagnetic and metallic one for CuO. This is because CuO is a strongly correlated system in which the strong electron-electron interactions should be considered in the calculations.

Since its establishment in the 1960's, Density Functional Theory (DFT) [30, 31] has become one of the most important tools for first principles calculations and has demonstrated its power in the study of the ground state properties of real materials.

Though exact in principle, some approximations must be adopted for the exchange-correlation expressions in practical calculations.

As the simplest and the first introduced approximation, the Local (Spin) Density Approximation (L(S)DA) [31-34] has reproduced the structural, electronic, magnetic and some other ground state properties of many materials satisfactorily. However, there are also some problems with this approximation. For instance, it overestimates the binding energies of many systems while underestimates atomic ground state energies, ionization energies and band gaps [35-38].

A natural progression to move beyond LSDA is the Generalized Gradient Approximation (GGA) [39-44] which makes gradient corrections to LSDA in consideration of the possible in-homogeneity of real electron systems. Although the introduction of GGA and various functionals could solve some open problems within LSDA and improve the power of DFT calculations to some extent [45-46], GGA enlarged very little the class of materials whose properties could be successfully described by DFT due to its semi-local nature. Therefore, there still remain some groups of materials whose properties cannot be accurately studied by the LSDA and GGA. One example is the strongly correlated systems which CuO belongs to. The reason why LSDA or GGA methods are not able to correctly describe this class of materials mainly consists in the fact that their energy functionals are built to treat the real interacting electron system as a (possibly homogeneous) electron gas, and thus result to be not accurate enough to deal with the situations in which strong localization of the electrons is likely to occur. In the last two decades, many new approaches have been proposed to

study this kind of systems with first principles calculations such as the self-interaction correction (SIC) method [35, 47], the GW approximation (GWA) [48-51]. One of the most popular approaches of this kind is LSDA+U [37, 52-61]. In this method, a mean field Hubbard-like term is added to the LSDA or GGA energy functions to improve the description of the electron correlations. The energy functional is generally taken from the Hubbard model [62] that represents the “natural” theoretical framework to deal with strongly correlated materials.

In the present work, the LSDA+U method implemented in the PAW method are applied to the study of the structural, electronic and magnetic properties of crystal CuO. As a comparison, we also present the results from the LSDA method. While the LSDA method predicts a metallic ground state for CuO, our results from the LSDA+U method shows that CuO is a semiconducting material with an indirect gap of about 1.0 eV, which agrees with experiments. The structural parameters and an antiferromagnetic ground state are also reproduced very well by using the LSDA+U method. We also investigate CuO with different native point defects by using the LSDA+U method and our study of the formations of these native point defects shows that CuO is an intrinsic p-type semiconductor.

The rest of this thesis is organized as follows. Chapter 2 is devoted to the description of theoretical foundations of our calculations. The density functional theory, its related approximations and techniques for practical calculations, and the LSDA+U method are discussed in this chapter. Then we show our results on the structural, electronic and magnetic properties of CuO in Chapter 3. In Chapter 4, CuO with

different native point defects is studied. Defect levels, structural relaxations and formation energies are examined. A conclusive discussion on the results of our work is presented in the last chapter together with some possible further work to be done.

CHAPTER 2

METHODOLOGY

First-principles calculations refer to quantum mechanical calculations which do not depend on any external parameters except the atomic numbers of the atoms involved in the calculations. In this chapter the theories, approximations and methods used in first principles calculations are described. The LSDA+U method implemented in the PAW approximation we adopted throughout this work is also described here.

2.1 Schrödinger Equation

Any problem in the electronic structure of matter is covered by the time-dependent Schrödinger equation

$$\hat{H}\Psi(R, r, t) = i\hbar \frac{\partial \Psi(R, r, t)}{\partial t} \quad (2.1)$$

where \hat{H} is the Hamiltonian operator corresponding to the total energy of the system, $\Psi(R, r, t)$ is the wavefunction, a function of all the self-variants of the system, including the nuclear positions R , electron positions and spins r and time t .

Suppose there are no external fields, the Hamiltonian of a system consisting of M nuclei (each with charge Z_α and mass m_α) and N electrons, in atomic units ($m_e = 1, e = 1, \hbar = 1$), is given by

$$\hat{H} = \hat{T} + \hat{V} \quad (2.2)$$

where

$$\hat{T} = -\frac{1}{2m_\alpha} \sum_\alpha \nabla_\alpha^2 - \frac{1}{2} \sum_i \nabla_i^2 \quad (2.3)$$

representing the kinetic energies of the nuclei and electrons respectively, and

$$\hat{V} = \sum_\alpha \sum_{\beta>\alpha} \frac{Z_\alpha Z_\beta}{|R_\alpha - R_\beta|} - \sum_\alpha \sum_i \frac{Z_\alpha}{|R_\alpha - r_i|} + \sum_i \sum_{j>i} \frac{1}{|r_i - r_j|} \quad (2.4)$$

describing the potential energies due to nuclear-nuclear repulsion, nuclear-electron attraction and electron-electron repulsion.

Since the Hamiltonian above is independent of time, using the technique of separation of variables the solution of the Schrödinger equation can be written as

$$\Psi(R, r, t) = \Psi(R, r) f(t). \quad (2.5)$$

By substituting this equation back to Equation (2.1), the time-dependent Schrödinger Equation is reduced to a time-independent Schrödinger Equation

$$\hat{H}\Psi = E\Psi \quad (2.6)$$

and

$$\Psi(R, r, t) = \Psi(R, r) \exp(-iEt / \hbar). \quad (2.7)$$

This equation shows that if the potential is independent of time and the system is in a state of energy E, all that is required to construct the time-dependent wavefunction

from the time-independent wavefunction is multiplication by $\exp(-iEt/\hbar)$, which is simply a modulation of its phase.

2.2 The Born-Oppenheimer Approximation

While theoretically the Schrödinger Equation is powerful to describe almost all the systems, it is very disappointing that in practice it is too complicated to be solved for all except the simplest systems. To overcome this difficulty, approximations have to be made. And the most common approximation is the Born-Oppenheimer Approximation [63, 64].

In the Born-Oppenheimer Approximation, the electrons and the ions in a real system are treated separately. This treatment is legitimate in most cases because of the large mass difference between the two families of particles. The forces on both electrons and nuclei due to their electric charge are of the same order of magnitude, and so the changes which occur in their momenta as a result of these forces must also be the same. One might therefore assume that the actual momenta of the electrons and nuclei were of similar magnitude. In this case, since the nuclei are so much more massive than the electrons, they must accordingly have much smaller velocities. Thus it is plausible that on the typical time scale of the nuclear motion, the electrons will very rapidly relax to the instantaneous ground state configuration. So that in solving the time independent Schrödinger equation resulting from the Hamiltonian in equation, we can assume that the nuclei are stationary and solve for the electronic ground state first and then calculate the energy of the system in that configuration and solve for the nuclear motion. This

separation of electronic and nuclear motion is known as the Born-Oppenheimer approximation.

Applying the Born-Oppenheimer approximation, the ionic wavefunction $\xi(\mathbf{R})$ is independent of the electronic wavefunction and the total wavefunction of the system can be approximately written as the product of ionic and electronic terms

$$\Psi(\mathbf{R}, \mathbf{r}) = \xi(\mathbf{R})\psi_{\mathbf{R}}(\mathbf{r}) \quad (2.8)$$

where the notation of the electronic wavefunction $\psi_{\mathbf{R}}(\mathbf{r})$ implies that it only depends parametrically on the ionic positions.

As a result of the Born-Oppenheimer Approximation, the Coulomb potential produced by the nuclei can be treated as a static external potential $V_{ext}(\mathbf{r})$

$$V_{ext}(\mathbf{r}_i) = -\sum_{\alpha} \frac{Z_{\alpha}}{|\mathbf{R}_{\alpha} - \mathbf{r}_i|}. \quad (2.9)$$

If we define

$$\hat{V}_{ext}(\mathbf{r}) = \sum_i V_{ext}(\mathbf{r}_i) \quad (2.10)$$

and

$$\hat{F} = -\sum_{i=1}^N \left(-\frac{1}{2}\nabla_i^2\right) + \sum_i \sum_{j>i}^N \frac{1}{|\mathbf{r}_i - \mathbf{r}_j|}, \quad (2.11)$$

then the Hamiltonian can be written as

$$\hat{H} = \hat{V}_{ext} + \hat{F}. \quad (2.12)$$

Since \hat{F} will be the same for all N-electron systems, the Hamiltonian and hence the ground state wave function $|\psi_0\rangle$ will be completely determined by N and \hat{V}_{ext} .

Therefore, the ground state wave function $|\psi_0\rangle$ and electronic charge density $\rho_0(r)$ are both functionals of the number of electrons N and the external potential $V_{ext}(r)$. The ground state electronic charge density in terms of $|\psi_0\rangle$ is

$$\rho_0(r_1) = N \int |\psi_0|^2 dr_2 \cdots dr_N. \quad (2.13)$$

2.3 Density Functional Theory

Separate treatment of electronic and ionic movements simplifies the original problems and allows us to treat the ions in a classical formalism. However, because of the mutual interactions between electrons, the electronic problem is still a far too complicated many body quantum problem to be solved exactly in practical computations. Owing to this difficulty, further developments are required to convert a many-body problem into many one-body problems for real materials. Density Functional Theory provides a framework for these developments.

Density Functional Theory, based on two theorems first proved by Hohenberg and Kohn [30] in the 1960's, makes it possible to describe the ground state properties of a real system in terms of its ground state charge density instead of the far more complicated wavefunction. This theory allows us to find the ground state properties of a system in terms of the ground state charge density without explicit recourse to many-particle wavefunctions. Since the electronic charge density depends only on four variables (three Cartesian variables and electron spin), the original $4M$ (where M is the number of electrons) variables problem involving the complicated wavefunctions is reduced to a much simpler problem in which only four variables are needed to define

the charge density at a point. Thus the computational efforts will be drastically reduced and the problem will be feasible to be solved computationally.

2.3.1 The Hohenberg-Kohn Theorems

The two Hohenberg-Kohn theorems state that:

Theorem I: For any system of interacting particles in an external potential $V_{ext}(r)$, the potential $V_{ext}(r)$ is determined uniquely, except for a constant, by the ground state electronic charge density $\rho_0(r)$.

Theorem II: A universal functional for the energy in terms of the density $\rho(r)$ can be defined, valid for any external potential $V_{ext}(r)$. For any particular $V_{ext}(r)$, the exact ground state energy of the system is the global minimum value of this functional, and the density $\rho(r)$ that minimizes the functional is the exact ground state density $\rho_0(r)$.

A schematic representation of these two theorems is shown in Figure 2.1.

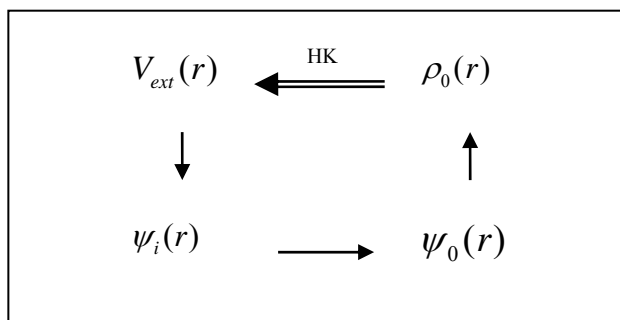


Figure 2.1 Schematic representation of Hohenberg-Kohn theorems. The single arrows denote the usual solution of the Schrödinger equation where the potential $V_{ext}(r)$ determines all states of the system $\psi_i(r)$, including the ground state $\psi_0(r)$ and ground density $n_0(r)$. The double arrow labeled “HK” denotes the Hohenberg-Kohn theorems, which completes the cycle. From [128].

The proofs of the Hohenberg-Kohn theorems are disarmingly simple. To prove Theorem I, we use the method of *reductio ad absurdum*: suppose that there was a second different external potential $V'_{ext}(r)$ which differs from $V_{ext}(r)$ by more than a constant. These two external potentials give rise to the same ground state density $\rho_0(r)$ but lead to two different Hamiltonians, \hat{H} and \hat{H}' , which have two different non-degenerate ground state wavefunctions, ψ and ψ' . Since ψ' is not the ground state wavefunction of \hat{H} , it follows that

$$\begin{aligned} E_0 &= \langle \psi | \hat{H} | \psi \rangle < \langle \psi' | \hat{H} | \psi' \rangle = \langle \psi' | \hat{H}' | \psi' \rangle + \langle \psi' | \hat{H} - \hat{H}' | \psi' \rangle \\ &= E'_0 + \int d^3r \left[V_{ext}(r) - V'_{ext}(r) \right] \rho_0(r) \end{aligned} \quad (2.14)$$

where E_0 and E'_0 are the ground state energies for \hat{H} and \hat{H}' , respectively. Similarly, if we consider E'_0 in exactly the same way, we have an equation

$$\begin{aligned} E'_0 &= \langle \psi' | \hat{H}' | \psi' \rangle < \langle \psi | \hat{H}' | \psi \rangle = \langle \psi | \hat{H} | \psi \rangle + \langle \psi | \hat{H}' - \hat{H} | \psi \rangle \\ &= E_0 - \int d^3r \left[V_{ext}(r) - V'_{ext}(r) \right] \rho_0(r). \end{aligned} \quad (2.15)$$

Adding these two equations, we would obtain the contradictory inequality

$$E_0 + E'_0 < E_0 + E'_0, \quad (2.16)$$

which is absurd. This shows that there cannot be two different external potentials differing by more than a constant which give the same ground state charge density.

The charge density uniquely determines N and the external potential $V_{ext}(r)$ within a constant. Because the external potential and number of electrons N determine all the ground state properties of the system since the Hamiltonian and

ground state wave function are determined by them. Hence all properties of the ground state, for example the kinetic energy $T[\rho]$, the potential energy $V[\rho]$ and the total energy $E[\rho]$, are uniquely determined by the charge density $\rho(r)$. Then we have, for the total energy

$$E[\rho] = T[\rho] + V_{ne}[\rho] + V_{ee}[\rho] = \int \rho(r)V(r)dr + F[\rho] \quad (2.17)$$

where

$$F[\rho] = T[\rho] + V_{ee}[\rho] \quad (2.18)$$

is an introduced functional as defined above.

The second Theorem can be easily proved by using the variational principle: by the first Theorem, a given electronic charge density $\rho(r)$ determines its own external potential $V_{ext}(r)$ and ground state wavefunction $\psi_0[\rho]$. If this wavefunction is used as a trial function for the Hamiltonian having external potential $V(r)$, then

$$\begin{aligned} \langle \psi_0[\rho] | \hat{H} | \psi_0[\rho] \rangle &= \langle \psi_0[\rho] | \hat{F} | \psi_0[\rho] \rangle + \langle \psi_0[\rho] | \hat{V} | \psi_0[\rho] \rangle \\ &= F[\rho] + \int \rho(r)V(r)dr = E_v[\rho] \geq E_v[\rho_0] = E_0 = \langle \psi_0[\rho_0] | \hat{H} | \psi_0[\rho_0] \rangle. \end{aligned} \quad (2.19)$$

For non-degenerate ground states, the equality holds only if

$$\psi_0[\rho] = \psi_0[\rho_0], \quad (2.20)$$

and therefore

$$\rho = \rho_0. \quad (2.21)$$

This shows that the ground state density is indeed the density that minimizes the functional.

The inequality follows from Rayleigh–Ritz’s variational principle for the wave function, but applied to the electronic density. Assuming differentiability of $E[\rho]$, the variational principle requires that the ground state density satisfy

$$\delta \left\{ E[\rho] - \mu \left[\int \rho_0(r) dr - N \right] \right\} = 0 \quad (2.22)$$

which gives the Euler-Lagrange equation of the form

$$\mu = \frac{\delta E[\rho_0]}{\delta \rho_0(r)} = V(r) + \frac{\delta F[\rho_0]}{\delta \rho_0(r)} \quad (2.23)$$

where μ is the Lagrange multiplier corresponding to the chemical potential associated with the constraint

$$\int \rho_0(r) dr = N. \quad (2.24)$$

Equation (2.23) is the basic working equation of density functional theory.

The above proofs assumed the non-degeneracy of the ground states. It has been shown that this condition can be lifted by the so-called “constrained search formulation” proposed by Levy [65-67] and Lieb [68-70] and therefore the density functional formalism can be generalized to deal with both non-degenerate and degenerate ground states.

$F[\rho]$ of equation (2.18) is a universal functional of $\rho(r)$ in a sense that $F[\rho]$ is defined independently of the external potential $V(r)$. If we knew the exact functional $F[\rho]$, the equation (2.22) would be an exact equation for the ground state electron density. Therefore, once we have an explicit form for $F[\rho]$, we can apply this method to any system. However, accurate implementations of the density functional

theory are far from easy to achieve because of the unfortunate fact that the functional $F[\rho]$ is hard to come by in explicit form.

2.3.2 The Kohn-Sham Method

Density functional theory is the most widely used method today for electronic structure calculations because of the approach proposed by Kohn and Sham in 1965 [31] to replace the original many-body problem by an auxiliary independent-particle problem. This is an ansatz that, in principle, leads to exact calculations of properties of many-body systems using independent-particle methods; in practice, it has made possible approximate formulations that have proved to be remarkably successful. As a self-consistent method, the Kohn-Sham approach involves independent particles but an interacting density, an appreciation of which clarifies the way the method is used.

The Kohn-Sham ansatz assumes that the exact ground state density $\rho_0(r)$ can be represented by the ground state density $\rho(r)$ of an auxiliary system of non-interacting particles as shown in Figure 2.2. Although there are no rigorous proofs for real systems of interest, it is assumed this equivalent non-interacting system does exist.

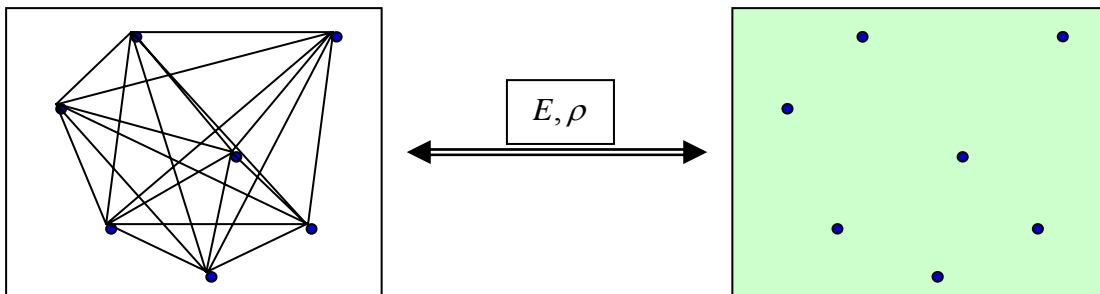


Figure 2.2 A cartoon representing the relationship between the real many body system (left hand side) and the auxiliary non-interacting system of Kohn-Sham method.

The auxiliary Hamiltonian is chosen to have the usual kinetic operator and an effective local potential $V_{eff}(r)$ acting on an electron but have no electron-electron repulsion terms. Using the atomic units, this Hamiltonian is written as

$$\hat{H}_s = \sum_i^N \left(\frac{1}{2} \nabla_i^2 \right) + \sum_i^N V_{eff}(r_i) \quad (2.25)$$

There will be an exact determinantal ground state wavefunction for this system,

$$\psi_s = \frac{1}{\sqrt{N!}} \det[\varphi_1 \varphi_2 \dots \varphi_N] \quad (2.26)$$

where the φ_i are called KS orbitals corresponding to the N lowest eigenstates of the one-electron Hamiltonian \hat{h}_s :

$$\hat{h}_s \varphi_i = \left[-\frac{1}{2} \nabla^2 + V_{eff}(r) \right] \varphi_i = \varepsilon_i \varphi_i \quad (2.27)$$

The electronic charge density will be given as

$$\rho(r) = \sum_{i=1}^N |\varphi_i(r)|^2 \quad (2.28)$$

and the kinetic term is

$$\begin{aligned} T_s[\rho] &= \langle \psi_s | \sum_{i=1}^N \left(-\frac{1}{2} \nabla_i^2 \right) | \psi_s \rangle \\ &= \sum_{i=1}^N \left\langle \varphi_i \left| -\frac{1}{2} \nabla^2 \right| \varphi_i \right\rangle \end{aligned} \quad (2.29)$$

Using this kinetic energy form, the universal functional $F[\rho]$ can be rewritten

as

$$\begin{aligned}
F[\rho] &= T[\rho] + V_{ee}[\rho] \\
&= T_s[\rho] + J[\rho] + \{T[\rho] - T_s[\rho] + V_{ee}[\rho] - J[\rho]\} \\
&= T_s[\rho] + J[\rho] + E_{xc}[\rho]
\end{aligned} \tag{2.30}$$

where $J[\rho]$ is the classical electrostatic interaction energy corresponding to a charge distribution $\rho(r)$,

$$J[\rho] = \frac{1}{2} \int \frac{\rho(r)\rho(r')}{|r-r'|} dr dr' \tag{2.31}$$

Equation (2.30) also defines the exchange-correlation energy as a functional of density

$$E_{xc}[\rho] = T[\rho] - T_s[\rho] + V_{ee}[\rho] - J[\rho] \tag{2.32}$$

from this definition, we can see clearly that the exchange-correlation energy $E_{xc}[\rho]$ includes two parts of contributions: the non-classical electron-electron interaction energy and the difference between the two kinetic energies $T[\rho]$ and $T_s[\rho]$.

Upon substitution of the expression of $F[\rho]$ in equation (2.17), the total energy functional can be rewritten as

$$E[\rho] = T_s[\rho] + J[\rho] + E_{xc}[\rho] + \int \rho(r)V(r)dr \tag{2.33}$$

and the Euler-Lagrange equation now becomes

$$\mu = V_{eff}(r) + \frac{\delta T_s[\rho]}{\delta \rho(r)} \tag{2.34}$$

where the Kohn-Sham effective potential is defined by

$$\begin{aligned}
V_{\text{eff}}(r) &= V(r) + \frac{\delta J[\rho]}{\delta \rho(r)} + \frac{\delta E_{xc}[\rho]}{\delta \rho(r)} \\
&= V(r) + \int \frac{\rho(r')}{|r-r'|} dr' + V_{xc}(r)
\end{aligned}
\tag{2.35}$$

with the exchange-correlation potential

$$V_{xc}(r) = \frac{\delta E_{xc}[\rho]}{\delta \rho(r)}
\tag{2.36}$$

In summary, the KS orbitals satisfy the well-known self-consistent Kohn-Sham equations

$$\left[-\frac{1}{2} \nabla^2 + V_{\text{eff}}(r) \right] \varphi_i = \varepsilon_i \varphi_i
\tag{2.37}$$

and the electronic charge density is constructed using the KS orbitals

$$\rho(r) = \sum_{i=1}^N |\varphi_i(r)|^2
\tag{2.38}$$

Comparing with the single Euler-Lagrange equation (2.34), we see that, by introducing the N KS orbitals, the Kohn-Sham equations handle $T_s[\rho]$, the dominant part of the true kinetic energy $T[\rho]$, indirectly but exactly. This is a major advance over the Hohenberg-Kohn theorems: the major part of the unknown functional $F[\rho]$ is known exactly; only a residual part $E_{xc}[\rho]$ is unknown now. The relationship between the Hohenberg-Kohn theorems and the Kohn-Sham method is schematically represented in Figure 2.3.

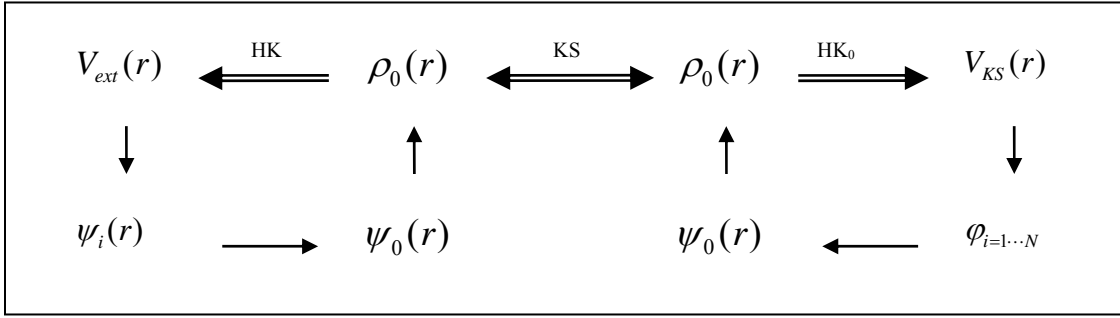


Figure 2.3 Schematic representation of Kohn-Sham method. The notation HK_0 denotes the Hohenberg-Kohn theorems applied to the non-interacting problem. The arrow labeled KS provides the connection in both directions between the many-body and single-particle systems. Therefore, in principle, solution of the single-particle Kohn-Sham problem determines all properties of the many-body system. From [128].

2.3.3 Spin Density Functional Theory

The density functional theory as it has been discussed up to this point only use the total density $\rho(r)$ as the fundamental variable. However, this is not the widely used density functional theory in practical applications. Much common is the spin density functional theory which works with two fundamental variables, i.e., the up and down spin densities $\rho^\alpha(r)$ and $\rho^\beta(r)$. They are defined as

$$\rho^\sigma(r) = \sum_{i=1}^{N_\sigma} |\varphi_i^\sigma(r)|^2 \quad \sigma = \alpha, \beta \quad (2.39)$$

with the interpretation that $\rho^\sigma(r)d^3r$ is the probability of finding an electron of spin σ in d^3r around r . These two fundamental variables then can be used to calculate the particle charge density $\rho(r)$ and spin-magnetization density $m(r)$ from

$$\rho(r) = \rho^\alpha(r) + \rho^\beta(r) \quad (2.40)$$

$$m(r) = \mu_B(\rho^\alpha(r) - \rho^\beta(r)) \quad (2.41)$$

where $\mu_B = eh/2m_e c$ is the Bohr magneton. Then the Hohenberg-Kohn Theorems can be proved, showing that the ground state wavefunction and all ground state observables are unique functionals of $\rho(r)$ and $m(r)$ or, equivalently, $\rho^\alpha(r)$ and $\rho^\beta(r)$. Similarly, the Kohn-Sham equations can be developed with spin-dependent effective potentials $V_{eff,\alpha}(r)$ as follows,

$$\left\{ \begin{array}{l} \left[-\frac{1}{2}\nabla^2 + V_{eff,\alpha}(r) \right] \varphi_{i,\alpha} = \varepsilon_{i,\alpha} \varphi_{i,\alpha} \\ \left[-\frac{1}{2}\nabla^2 + V_{eff,\beta}(r) \right] \varphi_{i,\beta} = \varepsilon_{i,\beta} \varphi_{i,\beta} \end{array} \right\} \quad (2.42)$$

where

$$\left\{ \begin{array}{l} V_{eff,\alpha}(r) \\ V_{eff,\beta}(r) \end{array} \right\} = V(r) + \int \frac{\rho(r')}{|r-r'|} dr' + \left\{ \begin{array}{l} \left(\frac{\delta E_{xc}[\rho^\alpha, \rho^\beta]}{\delta \rho^\alpha(r)} \right)_{\rho^\beta(r)} \\ \left(\frac{\delta E_{xc}[\rho^\alpha, \rho^\beta]}{\delta \rho^\beta(r)} \right)_{\rho^\alpha(r)} \end{array} \right\}, \quad (2.43)$$

$$\text{i.e.} \quad \left\{ \begin{array}{l} V_{eff,\alpha}(r) \\ V_{eff,\beta}(r) \end{array} \right\} = V(r) + \int \frac{\rho(r')}{|r-r'|} dr' + \left\{ \begin{array}{l} V_{xc,\alpha}(r) \\ V_{xc,\beta}(r) \end{array} \right\}. \quad (2.44)$$

Spin density functional theory is essential in the theory of atoms and molecules with net spins, as well as solids with magnetic order. In fact, all modern density functional calculations are spin density functional calculations.

2.4 Approximations of $E_{xc}[\rho]$: L(S)DA and GGA

The density functional theory as it has been discussed up to this point is exact and no approximation was introduced into this theory. However, the exchange

correlation energy functional $E_{xc}[\rho]$, though well defined and exact in principle, is not known exactly. Therefore, to make the density functional theory a practical tool for electronic calculations, we have to introduce approximation to express explicitly the exchange correlation energy functional $E_{xc}[\rho]$.

The simplest approximation of the exchange correlation energy is the local (spin) density approximation (L(S)DA) proposed by Kohn and Sham in 1965 [31]. The main idea of LSDA is that the real inhomogeneous electronic systems can often be regarded as locally homogeneous as the homogeneous electron gas having the same density. Thus, the exchange correlation energy is simply an integral over all space with the exchange correlation energy density ε_{xc}^h at each point,

$$\begin{aligned} E_{xc}^{LSDA}[\rho^\alpha, \rho^\beta] &= \int \rho(r) \varepsilon_{xc}^h(\rho^\alpha(r), \rho^\beta(r)) d^3r \\ &= \int \rho(r) [\varepsilon_x^h(\rho^\alpha(r), \rho^\beta(r)) + \varepsilon_c^h(\rho^\alpha(r), \rho^\beta(r))] d^3r \end{aligned} \quad (2.45)$$

in the second step ε_{xc}^h has been divided into two parts: an exchange part ε_x^h and a correlation part ε_c^h

$$\varepsilon_{xc}^h(\rho^\alpha(r), \rho^\beta(r)) = \varepsilon_x^h(\rho^\alpha(r), \rho^\beta(r)) + \varepsilon_c^h(\rho^\alpha(r), \rho^\beta(r)) \quad (2.46)$$

Since the exchange energy of the homogeneous gas has a simple analytical form and the correlation energy has been calculated to great accuracy using the Quantum Monte Carlo methods, we can obtain an explicit form for the exchange correlation energy based on this approximation and then we can solve the Kohn-Sham equations.

Although it is extremely simple, the LSDA is a very successful approximation for many systems of interest, not only for those where the electronic density is quite

homogeneous (these are the systems that the approximation was designed to work with), but also for less uniform systems where the electronic density is rapidly varying. However, there are also a number of problems with the LSDA [35-38]. For instance, it usually overestimates the bonding energies but underestimates the energy band gap.

To overcome these and other problems of LSDA, it is natural to improve the exchange correlation energy functional in LSDA by introducing a dependence on the gradient of the electron density, which is call the General Gradient Approximation (GGA) [39-44]. The GGA expression for the exchange correlation energy functional looks like

$$E_{xc}^{GGA}[\rho^\alpha, \rho^\beta] = \int \rho(r) \varepsilon_{xc}[\rho^\alpha, \rho^\beta] dr + \int F_{xc}[\rho^\alpha, \rho^\beta, \nabla \rho^\alpha, \nabla \rho^\beta] dr \quad (2.47)$$

where the functional F_{xc} is constructed under guidance of wave vector analysis of the exchange correlation energy to satisfy some formal conditions, such as the sum rule, the physical asymptotic behaviors and so on. Several expressions of the exchange correlation energy density have been described in different formulations of the GGA functionals.

GGA did improve the descriptions of some systems over LSDA. One of the famous examples is that GGA has predicted the correct ground state of bulk Fe to be ferromagnetic body-centered cubic structure [71], while the LSDA has predicted a wrong non-ferromagnetic face-centered cubic structure [72-75]. GGA also reproduces the binding energies, atomic energies and bond lengths better than LSDA. Nevertheless, there still exist some systems which cannot be properly described by GGA because of its semi-local nature. What is worse is that no systematic way has been developed to

improve the functionals for exchange and correlation. The problems are most severe in materials in which the electrons tend to be localized and strongly interacting, such as transition metal oxides and rare earth elements and compounds.

2.5 Strongly Correlated Systems and LSDA+U Method

Although there is no rigorous definition for the strongly correlated systems, they are often referred as those systems in which the interactions (correlations) among the constituent particles are very strong. Such systems usually contain transition metal or rare-earth metal ions with partially filled d or f shells.

As mentioned earlier and from abundant literature [76-79], LSDA as well as GGA fails in describing the electronic structure of strongly correlated systems. The failure can be traced back to the mean-field character of the Kohn-Sham equations as well as to the poor description of strong correlation effects within the homogeneous electron gas. The insufficient treatments of on-site strong Coulomb correlation effects are responsible for the breakdown of the LSDA and GGA descriptions of the electronic structure of these compounds.

Several attempts have been made to take into account the strong electron-electron correlation effects such as the self-interaction correction (SIC) method [35, 47], the Hartree-Fock (HF) method [80-83], the GW approximation (GWA) [48-51]. One of the most popular approaches is the LSDA+U method which was proposed by Anisimov *et al* [37] and reformulated later by some others [52-61]. In the LSDA+U method, the electrons are separated into two subsystems as in the Anderson model [84]: localized d or f electrons for which Coulomb d - d interaction should be taken into account and

delocalized s , p electrons which could be described by using an orbital-independent one-electron potential (LSDA). The total energy functional in the LSDA+U method is obtained by adding a Hubbard-like term [62] to the LSDA total energy functional, and at the same time, by subtracting the Coulomb energy of d - d interactions from the LSDA total energy functional.

In this thesis, we adopt a simple version of the LSDA+U method formulated by Dudarev *et al* [59, 60]. It is based on a model Hamiltonian with the form

$$H = \frac{U}{2} \sum_{m,m',\sigma} \hat{n}_{m,\sigma} \hat{n}_{m',-\sigma} + \frac{(U-J)}{2} \sum_{m \neq m',\sigma} \hat{n}_{m,\sigma} \hat{n}_{m',\sigma} \quad (2.48)$$

where $\hat{n}_{m,\sigma}$ is the operator yielding the number of electrons occupying an orbital with magnetic quantum number m and spin σ at a particular site; J is a parameter representing the screened exchange energy; and U is a spherically averaged Hubbard parameter describing the Coulomb-energy cost to place two d electrons at the same site

$$U = E(d^{N+1}) + E(d^{N-1}) - 2E(d^N). \quad (2.49)$$

Then the total energy functional can be written as

$$E^{LSDA+U} = E^{LSDA} + \frac{(U-J)}{2} \sum_{m,\sigma} (n_{m,\sigma} - n_{m,\sigma}^2). \quad (2.50)$$

This functional is yet not invariant with respect to a unitary transformation of the orbitals. To obtain a rotationally invariant energy functional, Lichtenstein *et al* [57] proposed to replace the number operator $\hat{n}_{m,\sigma}$ by the on-site density matrix $P_{mm'}^\sigma$ of the d electrons as follows

$$E^{LSDA+U} = E^{LSDA} + \frac{(U - J)}{2} \sum_{\sigma} Tr [P^{\sigma} - P^{\sigma} P^{\sigma}]. \quad (2.51)$$

The interpretation of this functional is particularly simple. In the limit of an idempotent on-site density matrix P^{σ}

$$P^{\sigma} = P^{\sigma} P^{\sigma}, \quad (2.52)$$

The LSDA+U energy functional yields exactly the same energy as the LSDA functional

$$E^{LSDA+U} = E^{LSDA}. \quad (2.53)$$

The one-electron potential is given by the functional derivative of the total energy with respect to the electron density. In a matrix representation, this can be formulated as

$$V_{ij}^{\sigma} = \frac{\delta E^{LSDA+U}}{\delta P_{ij}^{\sigma}} = \frac{\delta E^{LSDA}}{\delta P_{ij}^{\sigma}} + (U - J) \left[\frac{1}{2} \delta_{ij} - P_{ij}^{\sigma} \right]. \quad (2.54)$$

It can be seen that the potential becomes spin and orbital dependent after adding the on-site Coulomb interaction to the LSDA Hamiltonian. Because a larger energy cost is associated with fluctuations of the d occupancy, the orbital-dependent potential reduces the fluctuations of the d occupancy, resulting in a better justification of a mean field approach. The LSDA+U method has proven to be successful in applications to strongly correlated systems [37, 58-60, 85-87].

2.6 Solving the Kohn-Sham Equations

At this point, we can consider solving the Kohn-Sham equations to obtain the quantities we want. However, it is still a formidable task to handle an infinite number of non-interacting electrons moving in the static potential of an infinite number of nuclei or ions. There exist two difficulties: a wavefunction must be calculated for each of the

infinite number of electrons in the system, and since each electronic wavefunction extends over the entire solid, the basis set required to expand each wavefunction is infinite. To overcome these problems, we must invoke some theories and approximations to reduce the infinite systems to finite ones.

2.6.1 Bloch's Theorem and k Point Sampling

Although the pure crystal is infinite in principle, the constituent ions are supposed to be at rest in their equilibrium positions and form a periodically repeated structure. In this case the electrons can be considered to move in a static potential $V(r)$, which may be the Kohn-Sham effective potential. Because of the periodicity of the crystal structure, this potential is also periodic. In mathematic words, the potential satisfies

$$V(L+r) = V(r) \quad (2.55)$$

for all Bravais lattice vectors L .

The Bloch's theorem [88, 89] states that the one-electron wavefunctions of electrons moving in this type of potential can be chosen to have the form of plane wave times a function with the periodicity of the Bravais lattice:

$$\varphi_{nk}(r) = e^{ik \cdot r} u_{nk}(r) \quad (2.56)$$

where k is the wave vector related to the translational properties and n is the band index labeling different eigenstates corresponding to the same k , and

$$u_{nk}(L+r) = u_{nk}(r) \quad (2.57)$$

for all L in the Bravais lattice.

Combining the above two equations we obtain

$$\varphi_{nk}(\mathbf{r} + \mathbf{L}) = e^{i\mathbf{k} \cdot \mathbf{L}} \varphi_{nk}(\mathbf{r}). \quad (2.58)$$

From this equation, we see that the Bloch's theorem have changed the problem of calculating an infinite number of electronic wavefunctions to one of calculating a finite number of electronic wavefunctions at an infinite number of k points.

On the other hand, the wave vector k can always be confined to the first Brillouin zone or to any other convenient primitive cell of the reciprocal lattice. This is because any k' not in the first Brillouin zone can be written as

$$k' = k + G \quad (2.59)$$

where k does lie in the first Brillouin zone and G is a reciprocal lattice vector defined by

$$G \cdot L = 2\pi m \quad (m \text{ is an integer}) \quad (2.60)$$

for all lattice vectors L . Thus we can restrict our attention to those k vectors which lie within the first Brillouin zone. The k points required in the electronic states calculations can be further reduced by the use of a small special set of k points in the first Brillouin zone, which is based on the fact that the electronic wavefunctions and other properties at k points that are very close together will be almost identical. Different methods [90-92] have been devised to choose the special points for obtaining very accurate approximation to the electronic potential and the total energy. The magnitude of any error due to the selection of special k points can always be reduced by choosing a denser set of k points.

2.6.2 Plane Wave Basis Sets and Pseudopotential Approximation

Solving the Kohn-Sham equations is an integral-differential problem, which is hard to attack in practical calculations. Therefore, it is necessary to transform this problem into an easier one. This can be achieved by expanding the electronic wavefunctions with a basis set. The plane wave basis set [93] seems a natural choice since the Bloch's theorem states that the electronic wavefunctions at each k point can be expanded in terms of a discrete plane wave basis set. In addition, plane wave basis sets offer many advantages in density functional calculations for solids, including completeness, an unbiased representation (parameter free), arbitrarily good convergence accuracy and the ability to use the Fast Fourier Transform (FFT) to move back and forth between real and reciprocal spaces.

In principle, to obtain exact expansions of the electronic wavefunctions, an infinite plane wave set is required. But in practice, it is impossible because we can only handle a finite number of plane waves. Thus the plane wave set is usually truncated to include only plane waves that have kinetic energies less than some particular cutoff energy E_{cut} :

$$\frac{\hbar^2}{2m}|k + G|^2 \leq E_{cut}. \quad (2.61)$$

In this way, a finite plane wave basis set is produced. The truncation of the plane wave basis set at a finite cutoff energy will certainly lead to the accuracy problems in the computed results. But it is possible to reach the accuracies we want by increasing the value of the cutoff energy until the calculated results have converged.

However it is still computationally too difficult in the real calculations even after the above methods and approximations are introduced. This is because a large number of plane waves are required to model accurately the core wavefunctions which oscillate rapidly with many nodes. A possible way to overcome this difficulty is the pseudopotential approximation [94-101] which is based on the fact that most physical properties of solids are dependent on the valence electrons to a much greater extent than on the core electrons. The pseudopotential method removes the core electrons and replaces them and the strong Coulomb potential by a much weaker pseudopotential and replaces the valence electron wavefunctions with a set of pseudo, smoothly varying wavefunctions which have no radial nodes in the core region. By doing so, the number of plane waves needed to expand the electronic wavefunctions is reduced significantly and fewer electronic wavefunctions have to be calculated because of the removal of the core electrons.

The pseudopotential approximation, especially the Vanderbilt's ultrasoft pseudopotential [101] approach is now widely used in the electronic structure calculations [102-106]. But the success of the method is partly hampered by the rather difficult generation of the pseudopotentials. It is also reported that the pseudopotentials fail in spin-polarized calculations for materials with a large magnetic moment [107].

2.6.3 The Projector Augmented Wave (PAW) Method

Some of the disadvantages of the pseudopotential method can be avoided in the all electron projector augmented wave (PAW) method [107-109] proposed by Blöchl. This method combines the ideas of the pseudopotential [94-101] and linearized

augmented plane wave (LAPW) [110-113] methods. In the PAW method, the all-electron (AE) wavefunction is constructed from a pseudo (PS) wavefunction and atom-like functions localized near the nuclei. The PS wavefunction $|\tilde{\varphi}\rangle$ coincides with the AE wavefunction $|\varphi\rangle$ in the interstitial region, i.e., outside the atomic regions. Inside the atomic region, or called augmentation region, the wavefunction is almost atom-like because the effect of the surrounding crystal is small. Therefore, a natural choice is to use solutions $|\phi_\Lambda\rangle$ of Schrödinger equation for the isolated atom, the so-called AE partial waves, as a basis set for the augmentation region. Here $\Lambda = \{t, n, l, m\}$ is a global index for the atom t , the angular momentum l , the magnetic quantum number m , and the index n , the energy for which Schrödinger equation is solved. Then the AE wavefunction is related to the PS wavefunction through a linear transformation:

$$|\varphi_n\rangle = |\tilde{\varphi}_n\rangle + \sum_{\Lambda} (|\phi_\Lambda\rangle - |\tilde{\phi}_\Lambda\rangle) \langle \tilde{p}_\Lambda | \tilde{\varphi}_n \rangle \quad (2.62)$$

where $|\tilde{\phi}_\Lambda\rangle$ is introduced PS partial wavefunctions which are centered on the atom. They are equivalent to the AE partial waves $|\phi_\Lambda\rangle$ outside their augmentation regions and match continuous onto $|\tilde{\phi}_\Lambda\rangle$ inside the augmentation regions. The projector functions $\langle \tilde{p}_\Lambda |$ are dual to the PS partial waves:

$$\langle \tilde{p}_\Lambda | \tilde{\phi}_{\Lambda'} \rangle = \delta_{\Lambda\Lambda'}. \quad (2.63)$$

The first term in equation (2.62) represents the PS wavefunction defined over the entire space, which is equal to the AE wavefunction in the interstitial region, and

which is expanded in plane waves. The second term is the AE partial wave expansions, which describes the correct nodal behavior of the wavefunction in the augmentation region. The third term eliminates the spurious contribution of the PS wavefunction in the augmentation region.

From equation (2.62), the AE charge density can be obtained:

$$\rho(r) = \tilde{\rho}(r) + \rho^1(r) - \tilde{\rho}^1(r) \quad (2.64)$$

where $\tilde{\rho}(r)$ is the pseudo charge density related directly to the PS wavefunctions $|\tilde{\varphi}_n\rangle$

$$\tilde{\rho}(r) = \sum_n f_n \langle \tilde{\varphi}_n | r \rangle \langle r | \tilde{\varphi}_n \rangle \quad (2.65)$$

with f_n defined as orbital occupation numbers for the nth state.

The onsite charge densities $\rho^1(r)$ and $\tilde{\rho}^1(r)$ are only defined inside the augmentation regions of each atom. They are defined as

$$\rho^1(r) = \sum_{(\Lambda, \Lambda')} P_{\Lambda, \Lambda'}^{PAW} \langle \phi_\Lambda | r \rangle \langle r | \phi_{\Lambda'} \rangle, \quad (2.66)$$

$$\tilde{\rho}^1(r) = \sum_{(\Lambda, \Lambda')} P_{\Lambda, \Lambda'}^{PAW} \langle \tilde{\phi}_\Lambda | r \rangle \langle r | \tilde{\phi}_{\Lambda'} \rangle. \quad (2.67)$$

The matrix $P_{\Lambda, \Lambda'}^{PAW}$ describes the occupancies of each augmentation channel (Λ, Λ') and is calculated from the PS wavefunctions applying the projector functions:

$$P_{\Lambda, \Lambda'}^{PAW} = \sum_n f_n \langle \tilde{\varphi}_n | \tilde{p}_\Lambda \rangle \langle \tilde{p}_{\Lambda'} | \tilde{\varphi}_n \rangle. \quad (2.68)$$

Generally speaking, the PAW potentials are more accurate than the pseudopotentials. This is because that firstly the radial cutoffs (core radii) are smaller than the radii used for the pseudopotentials. Thus the required energy cutoffs and basis

sets are somewhat larger. Secondly, the PAW potentials reconstruct the exact valence wavefunctions with all nodes in the core region through the cut-and-paste way as given by equation (2.62).

2.6.4 Implementation of LSDA+U within PAW Method

To derive the LSDA+U method within the PAW method, one needs to define the orbital density matrix $P_{mm'}$. The natural definition is based on the AE charge density inside the augmentation regions, $\rho^l(r)$, which can be written more explicitly as [86, 87]

$$\rho^l(r) = \sum_{lmn,l'm'n'} P_{lmn,l'm'n'}^{PAW} \langle \phi_{lmn} | r \rangle \langle r | \phi_{l'm'n'} \rangle \quad (2.69)$$

with the restriction to l and $l' = 2(d \text{ electrons})$, one can therefore relate the on-site density matrix $P_{mm'}$ to the PAW on-site occupancy matrix $P_{lmn,l'm'n'}^{PAW}$ through

$$P_{mm'} = \sum_{nn'} P_{lmn,l'm'n'}^{PAW} \langle \phi_{lmn} | \phi_{l'm'n'} \rangle. \quad (2.70)$$

This establishes the crucial link between the PAW and the LSDA+U method.

The total energy then has the form

$$\begin{aligned} E = E^{LSDA} &+ \frac{1}{2} \sum_{i,\sigma} \sum_{i,j,k,l} \langle \chi_i^t, \chi_k^t | V_{ee} | \chi_j^t, \chi_l^t \rangle P_{i,j}^{t,\sigma} P_{k,l}^{t,-\sigma} \\ &+ \frac{1}{2} \sum_{i,\sigma} \sum_{i,j,k,l} \left(\langle \chi_i^t, \chi_k^t | V_{ee} | \chi_j^t, \chi_l^t \rangle - \langle \chi_i^t, \chi_k^t | V_{ee} | \chi_l^t, \chi_j^t \rangle \right) P_{i,j}^{t,\sigma} P_{k,l}^{t,\sigma} \\ &- \sum_t \left[\frac{1}{2} U \sum_{\sigma,\sigma'} \mathbb{N}^{t,\sigma} (N^{t,\sigma'} - \delta_{\sigma\sigma'}) - \frac{1}{2} J \sum_{\sigma} \mathbb{N}^{t,\sigma} (N^{t,\sigma} - 1) \right] \end{aligned} \quad (2.71)$$

where $\mathbb{N}^{t,\sigma} = \sum_i P_{i,i}^{t,\sigma}$ is the average occupation of the d shell for each spin direction as

obtained from the d-orbital occupancies $P_{i,j}^{t,\sigma}$. The expressions $\langle \chi_i^t, \chi_k^t | V_{ee} | \chi_j^t, \chi_l^t \rangle$ are

the four-center matrix elements of the screened Coulomb interaction V_{ee} . Here the addition energy is applied only to the valence electrons, which are re-optimized while constrained to remain orthogonal to the core states.

2.6.5 The Self-Consistent Procedure

The solution of Kohn-Sham equations has to be obtained by an iterative, self-consistent procedure. The reason is that the effective potential $V_{eff}(r)$ depends on the density $\rho(r)$, which we are solving for. This procedure begins with initially guessed charge densities $\rho^\alpha(r)$ and $\rho^\beta(r)$, constructs the KS effective potentials from equation (2.43), and then finds the new output charge densities from equations (2.42) and (2.39) to begin another loop until the input and output charge densities are self-consistent. Then the interested quantities can be computed from the self-consistent charge densities or wavefunctions.

This self-consistent loop is shown schematically in Figure 2.4.

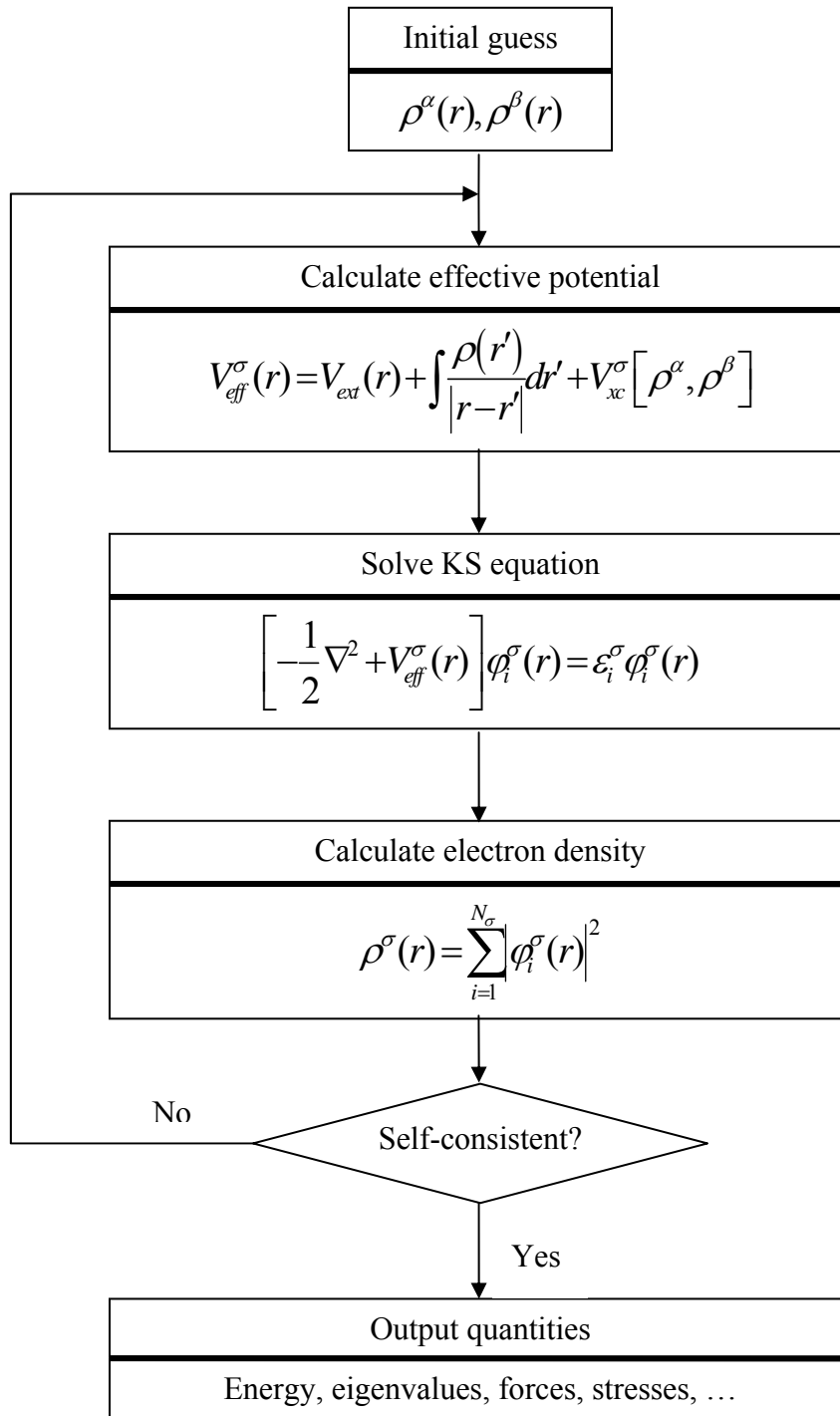


Figure 2.4 Schematic representation of the self-consistent loop to solve the Kohn-Sham equations. Adapted from [128].

CHAPTER 3
STRUCTURAL, ELECTRONIC AND MAGNETIC
PROPERTIES OF CRYSTAL CuO

In this chapter, the structural, electronic and magnetic properties of crystal CuO are studied by using the LSDA+U method. As a comparison, the electronic structure is also calculated by the LSDA method.

3.1 Computational Details

The calculations in this thesis were all performed using the Vienna Ab-initio Simulation Package (VASP) [107, 114-117]. VASP is a complex software package for performing *ab initio* quantum mechanics molecular dynamics simulations using pseudopotentials [94-101] or the PAW potentials [107-109] on plane wave basis sets. The approach implemented in VASP treats exchange and correlation based on density functional theory.

In order to reduce the number of plane wave basis functions necessary for accurately describing electronic wave functions, the PAW potentials implemented in the LSDA+U method in VASP by Kresse and Joubert [107] were used in this work to describe the electron-ion interactions. The PAW potential for Cu was generated from the atomic configuration of $[\text{Ar}]3d^{10}4s^1$. The 3d and 4s electrons were treated as valence

electrons. For O, the atomic configuration to generate the PAW potential was $[\text{He}]2s^22p^4$ and the 2s and 2p electrons were considered as valence electrons. At the level of the LSDA, the exchange-correlation functional proposed by Perdew and Zunger [35] based on the quantum Monte Carlo calculations of Ceperley and Alder [118] is used.

In both the LSDA and LSDA+U methods applied to the calculations in this section, the special k -point set is generated by the Γ centered Monkhorst-Pack scheme [92] with a density of $8 \times 8 \times 8$. The plane wave energy cutoff is set at 500 eV (36.75 Ry) to ensure the convergence of the calculations. For the LSDA+U calculations, we adopted the simplified rotationally invariant approach proposed by Dudarev *et al* [59, 60]. The values of U and J for Cu are set at 7.5 eV and 0.98 eV, respectively. We adopted these values from Reference [37], where the values were obtained from a “constrained LDA calculation” [119].

3.2 Crystal Structure

In order to check both the PAW potentials and the LSDA+U method we adopted in this work, calculations were performed to determine the crystal structure of cupric oxide. The crystal structure of CuO has been studied by x-ray diffraction [17, 120, 121] and it is found that, unlike the usual rocksalt structure of other 3d transition-metal monoxides, CuO crystallizes in a monoclinic tenorite structure with $C2/c$ symmetry. The unit cell containing four formula units is shown in Figure 3.1. The copper ions occupy positions $\pm(1/4, 1/4, 0; 3/4, 1/4, 1/2)$ along the lattice vectors a, b, c , respectively,

and the oxygen ions take positions $\pm(0, u, 1/4; 1/2, u + 1/2, 1/4)$, where u is a parameter describing the relative positions of oxygen ions along lattice vector b .

Due to its complex monoclinic structure, the unit cell shape, lattice vectors and atomic coordinates were relaxed simultaneously at a series of fixed volumes and the total energies were calculated for each volume. The optimized structural parameters corresponding to the lowest energy are listed in Table 3.1, along with experimental values and the percentage differences between them. From Table 3.1 we can see that the agreements between the experimental values and our calculated values are excellent, demonstrating that both the PAW potentials and the LSDA+U method we adopted are suitable for further study of CuO.

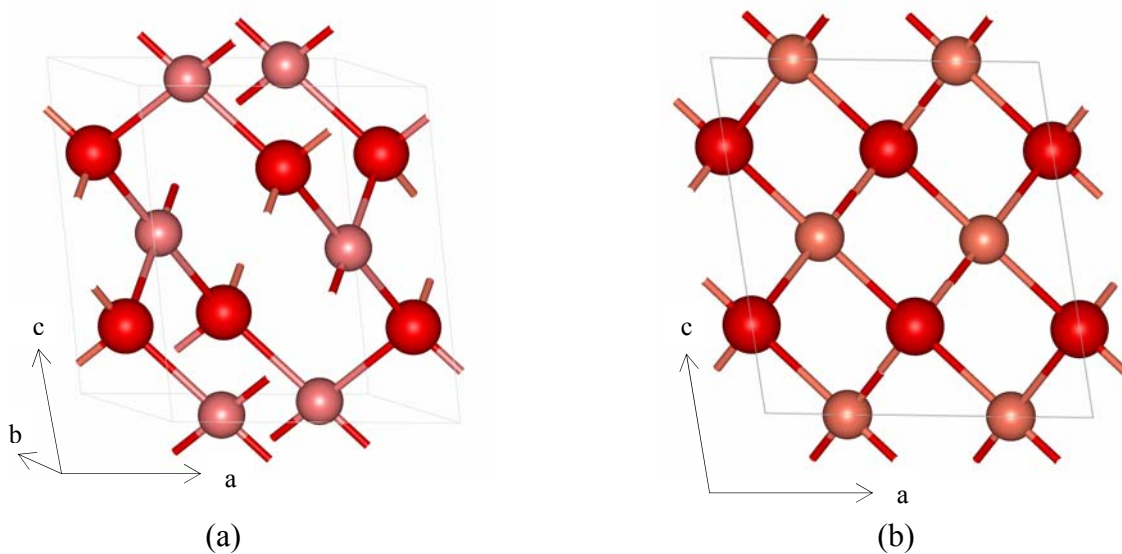


Figure 3.1 The crystal structure of cupric oxide. Black circles indicate O atoms, while grey circles indicate Cu atoms. (a) Side view. (b) Top view along the b axis.

Table 3.1 Calculated structural parameters for unit cell of CuO and their comparisons with experimental results. β is the angle between lattice vectors a and c in the monoclinic cell and u is a parameter describing the relative positions of O atoms along lattice vector b .

Parameter	Experiment *	Theoretical (This work)	Percentage Difference
a	4.653 Å	4.55 Å	2.17%
b	3.41 Å	3.34 Å	2.10%
c	5.108 Å	4.99 Å	2.31%
u	-0.584	-0.582	0.34%
β	99.483°	99.507°	0.024%

* Reference 122.

3.3 Electronic Structure

Using the optimized structural parameters for the perfect crystal, the electronic structure, including the band structure and density of states (DOS), of cupric oxide is calculated by using the LSDA+U method. To find out the effects of the introduced Hubbard U on this system, the electronic structure is also calculated by LSDA method, using the same optimized structural parameters and energy cutoffs.

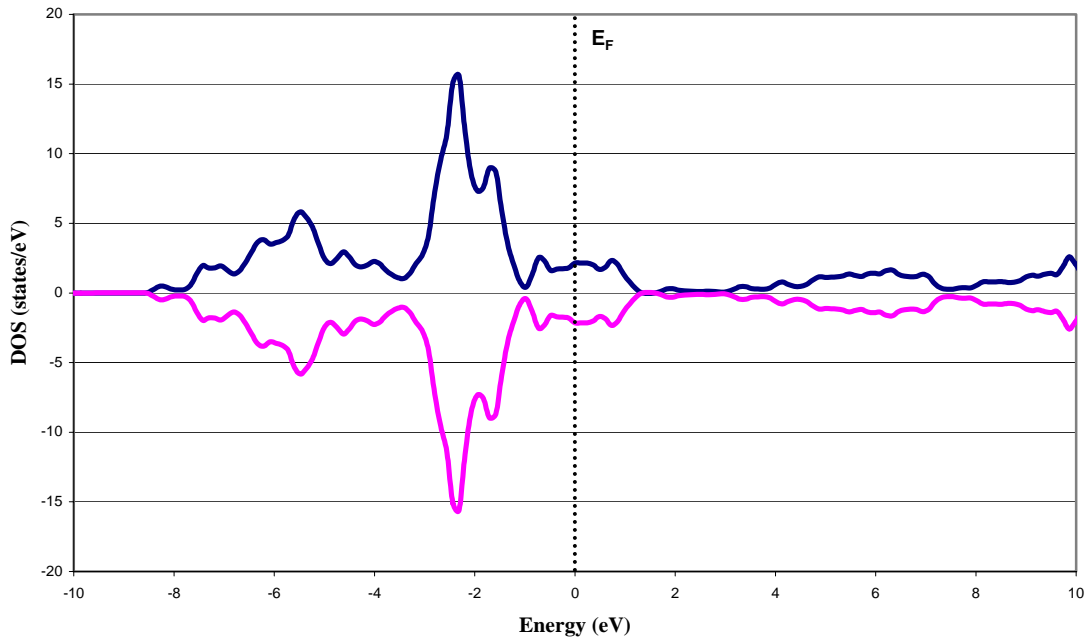


Figure 3.2 Density of states calculated using the LSDA method. The Fermi level is set at 0 eV. The majority is plotted upward; the minority is plotted downward.

The density of states of CuO from the calculations based on the LSDA and the LSDA+U methods are shown in Figure 3.2 and 3.3, respectively. The DOS calculated from LSDA method (Figure 3.2) exhibit a metallic character in that the spin densities states are crossed by the Fermi level. This is in contradiction to many experiments, where CuO is found to be a semiconducting material [8, 18-20]. On the other hand, the LSDA+U approach leads to a different picture of the DOS of CuO (Figure 3.3). No density states crossed the Fermi surface and an energy gap of about 1.0 eV is obtained. Thus within the LSDA+U method, CuO is a semiconductor, which agrees well with the experiments, but is totally different from the conclusion within the LSDA method.

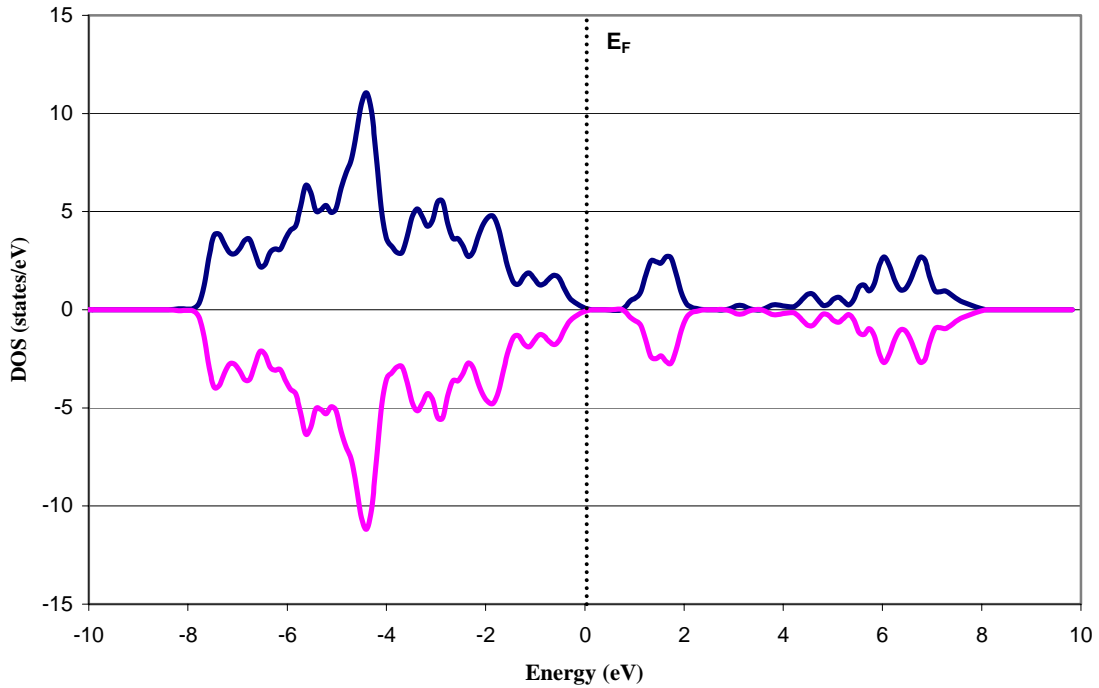


Figure 3.3 Density of states calculated using the LSDA+U method for CuO. The Fermi level is set at 0 eV. The majority is plotted upward; the minority is plotted downward. The symmetric filling of both majority and minority electrons indicates an antiferromagnetic ground state.

The above results can be seen more clearly in the band structures of CuO. The band structures of CuO along high-symmetry directions of the first Brillouin zone calculated by using the LSDA and LSDA+U methods are shown in Figure 3.5 and 3.6, respectively. The first Brillouin zone of the monoclinic structure is shown below in Figure 3.4. The notations of the high-symmetry points of the first Brillouin zone are followed from Reference [123] where

$$\Gamma = (000); B = (\frac{\bar{1}}{2} 00); Y = (0 \frac{1}{2} 0); Z = (00 \frac{1}{2}); C = (0 \frac{1}{2} \frac{1}{2}); D = (\frac{\bar{1}}{2} 0 \frac{1}{2}); A = (\frac{\bar{1}}{2} \frac{1}{2} 0), (\frac{\bar{1}}{2} \frac{\bar{1}}{2} 0),$$

$$\text{or}(\frac{1}{2} \frac{1}{2} 0); E = (\frac{\bar{1}}{2} \frac{1}{2} \frac{1}{2}), (\frac{\bar{1}}{2} \frac{\bar{1}}{2} \frac{1}{2}), \text{or}(\frac{1}{2} \frac{1}{2} \frac{1}{2}).$$

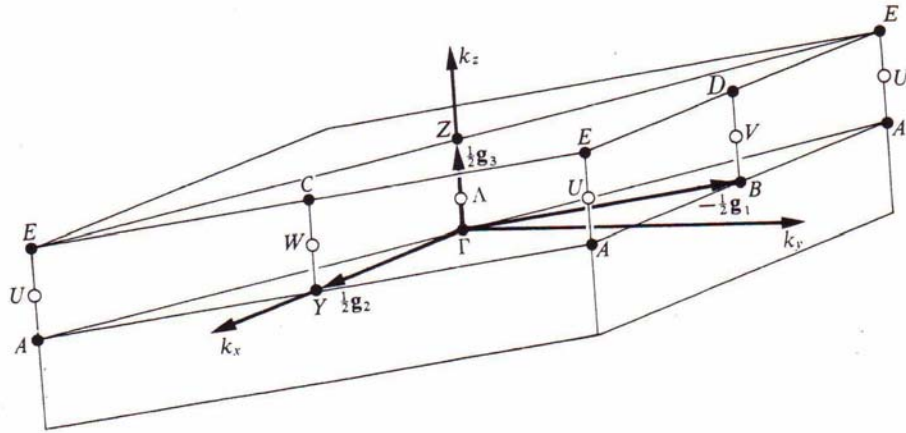


Figure 3.4 The first Brillouin zone of monoclinic structure.

In general, the band structures of CuO calculated from the LSDA and the LSDA+U methods are very similar. But they do have some differences, especially in the vicinity of the Fermi level. From Figure 3.5, we can clearly see that three electronic levels crossed the Fermi surface, which is set at 0. Thus there is no energy gap and CuO is predicted to have a metallic or semi-metallic ground state by the LSDA method. The band structure calculated by the LSDA method (Figure 3.5) is similar to the band structure of CuO calculated previously by the orthogonalized linear combination of atomic orbitals method (OLCAO) [29].

On the other hand, the band structure by the LSDA+U method (Figure 3.6) shows no electronic levels crossed by the Fermi surface. The three electronic levels crossed by the Fermi surface in the LSDA calculations have been shifted away from the

Fermi surface by introducing the Hubbard U , thus opening an indirect energy gap of about 1.0 eV and predicting a semiconducting ground state for CuO, which is the correct ground state obtained by many experiments [8, 18-20]. Our calculated energy gap 1.0 eV is also close to the experimental value 1.2-1.9 eV [4-8]. The indirect nature of the band gap is confirmed by some experiments [6, 19].

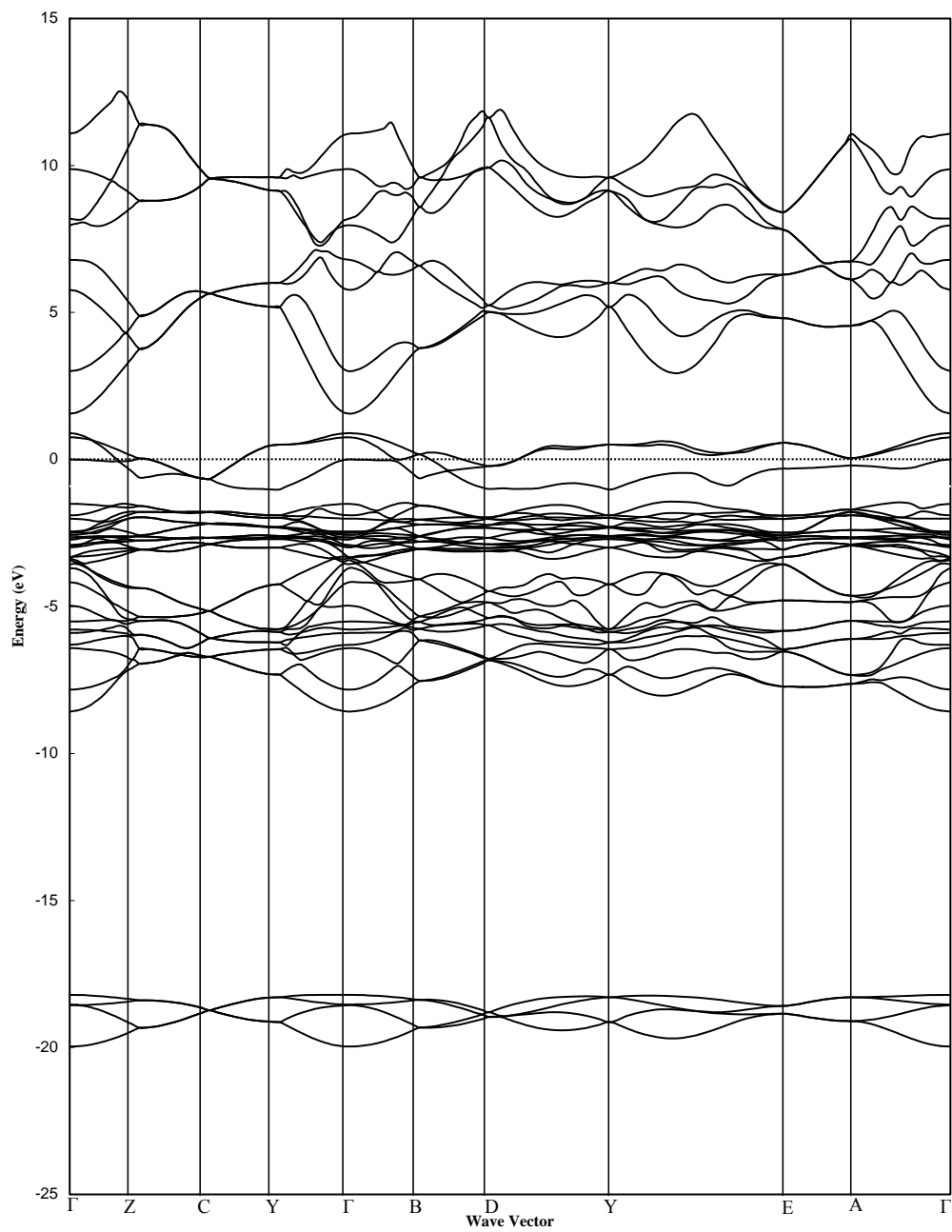


Figure 3.5 Band structure of CuO calculated using the LSDA method. The Fermi level is set at 0 eV.

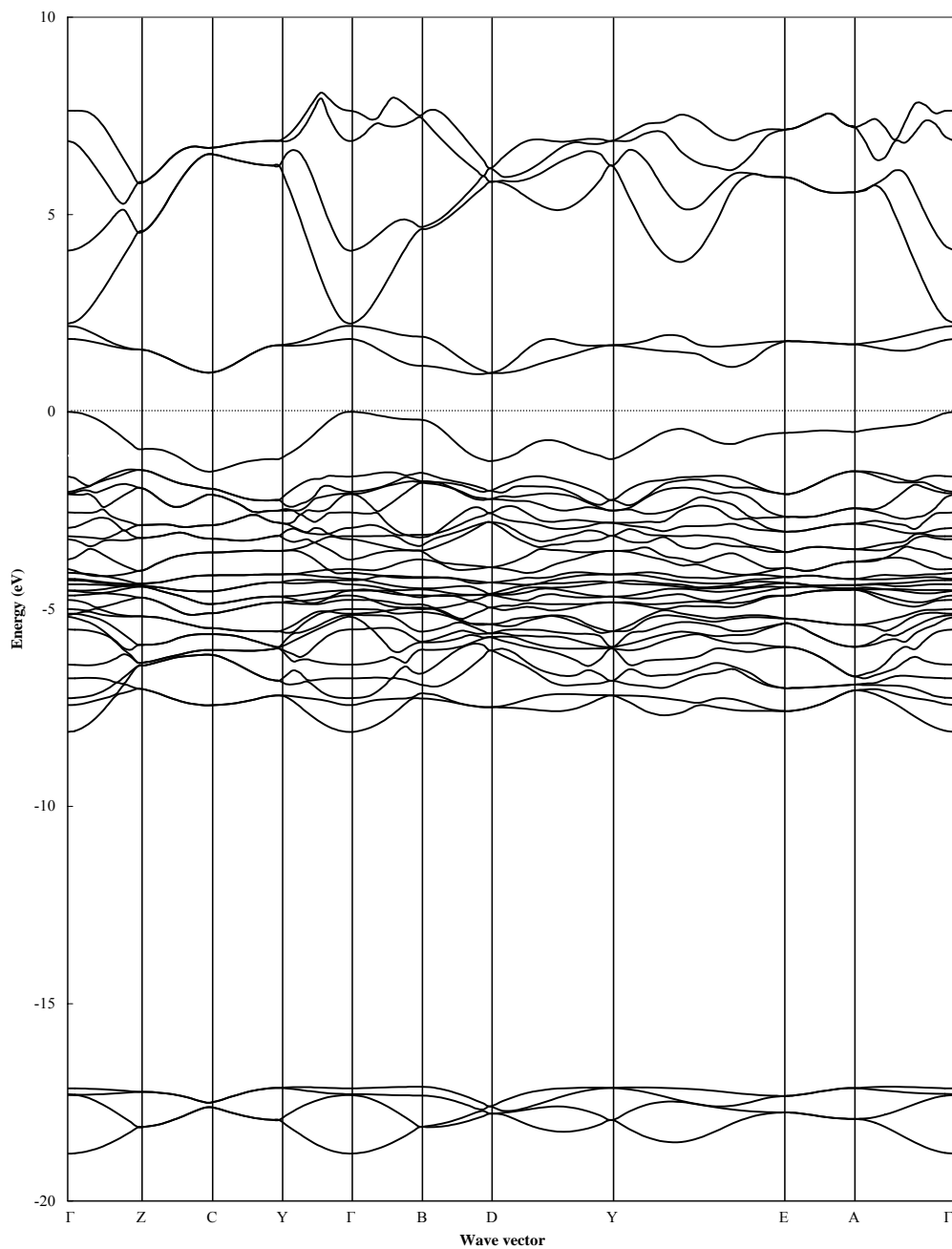


Figure 3.6 Band structure of CuO calculated using the LSDA+U method. The Fermi level is set at 0 eV.

3.4 Magnetic Properties

To find the magnetic properties of CuO in its ground state, all possible initial magnetic moments corresponding to the ferromagnetic, antiferromagnetic and non-magnetic (paramagnetic) cases were assigned to the four Cu atoms in the unit cell. Then the unit cell was allowed to relax and total energies of each initial setting were obtained. We found that the lowest energies correspond to the antiferromagnetic case with spin alignments shown in Figure 3.7 (the unit cell with totally reversed spin alignments also has the same lowest energy). The antiferromagnetic ground state and the spin alignments of the four Cu atoms from our calculations agree with the results from the experiments [22, 23, 124], where CuO is found to be antiferromagnetic below 221.5K with the same spin alignments as our calculations.

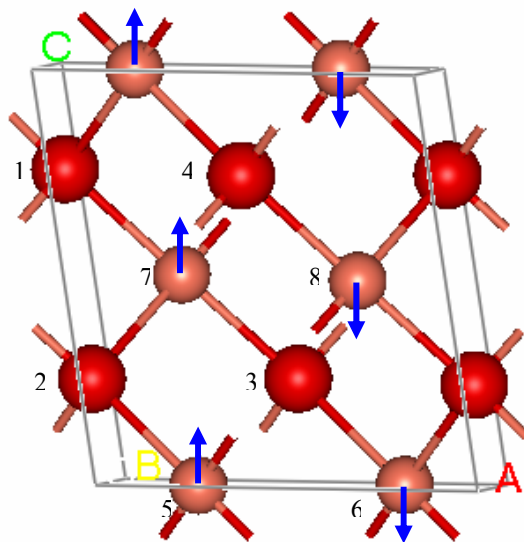


Figure 3.7 The unit cell of CuO with spin alignments corresponding to the lowest total energy. For the same lowest energy, the spin alignments could be totally reversed. Black circles indicate O atoms, while grey circles indicate Cu atoms. The atoms are numbered for the convenience of differentiating in Table 3.2 later.

Table 3.2 Decomposed magnetic moments in μ_B of atoms in the unit cell of CuO. The numbers of ions are assigned as shown in Figure 3.7.

# of ion	s	p	d	total
1	0	-0.006	0	-0.006
2	0	0.004	0	0.004
3	0	0.004	0	0.004
4	0	-0.006	0	-0.006
5	-0.004	-0.005	0.608	0.599
6	0.004	0.005	-0.606	-0.597
7	-0.004	-0.006	0.611	0.601
8	0.004	0.006	-0.609	-0.599
total	0	-0.004	0.005	0.001

After the antiferromagnetic ground state with the particular spin directions shown in Figure 3.7 was obtained, we have calculated the decomposed magnetic moments of each ion, which is listed in Table 3.2. From this table, we can see that the local magnetic moment per unit formula from our calculation is about $0.60 \mu_B$. The local magnetic moment from our calculations has a big difference with the value from previous calculations by Manabu Takahashi and Jun-ichi Igarashi [125]. In their calculations using the three-body scattering approximation on a multi-orbital tight-binding model, the local spin moments of Cu ions and O ions are $0.743 \mu_B$ and 0.107

μ_B , respectively. However, our first-principles result is in good agreement with the experimental value $0.5 \mu_B \sim 0.68 \mu_B$ [21-24, 124].

3.5 Discussion

While the LSDA method predicts a wrong non-magnetic and metallic ground state for CuO, the LSDA+U method using the PAW potentials in the present work makes important improvements over the LSDA method by predicting CuO correctly with an antiferromagnetic and semiconducting ground state, in good agreement with experiments. The structural parameters from our calculations are only within a few percents with the experimental values ranging from 1.2 to 1.9 eV. The electronic structure obtained in our LSDA+U calculations shows that CuO is a semiconductor with an indirect energy gap of about 1.0 eV. The indirect gap is confirmed by many experiments and the value of 1.0 eV is also close to the experimental values. The spin orderings of Cu atoms and the local magnetic moments per unit formula in the obtained antiferromagnetic ground state from our calculations also agrees very well with experimental results.

CHAPTER 4

NATIVE POINT DEFECTS IN BULK CuO

Native point defects are defects intrinsic to the semiconductors. They play a very important role in semiconductors, both fundamentally and practically. In this chapter, we have studied the structural relaxations and defect levels induced by various native point defects in CuO. The formation energies of these defects are also calculated using the total energies of the supercells. By comparing the formation energies, it is concluded that Cu vacancies are most stable defect in CuO and thus CuO is intrinsically a p-type semiconductor.

4.1 Computational Details

The calculations in this section are carried out using the supercell method with the LSDA+U method of the simplified rotationally invariant approach as we did in the previous chapter. The values of U and J are the same as those used in the last chapter. A plane wave cutoff energy of 400 eV (29.4 Ry) is used in these calculations.

4.1.1 Supercell Geometry

For calculations on a system that contains a single defect, a continuous and infinite number of plane wave basis states would be required since the Bloch theorem cannot be applied to this system. However it is impossible to use an infinite number of

basis set in practical calculations. To overcome this difficulty, the supercell geometry is introduced. In the supercell geometry, the defect surrounded by a region of perfect crystal is constructed as the supercell, containing usually much more atoms than a unit cell does, and the whole structure (supercell) is periodically repeated throughout the space. A major advantage using the supercell is that we can perform the numerical integrations over Brillouin zone only at the Γ point. Because the first Brillouin zone is inversely proportional to the cell, enlarging the cell will reduce the size of the first Brillouin zone. When the supercell approaches to the limit of infinitely large, the first Brillouin zone shrinks into one point – the Γ point. This is important in two aspects: first, the larger the supercell size, the closer our results will be to the case of a single isolated defect. When the supercell is infinite, the defect becomes a truly isolated defect because there are no interactions between defects in neighboring supercells. Second, at Γ point, $k=0$, the Bloch wave function is a real function in stead of a complex function in other k points. This will reduce the computational efforts significantly. Practically, we cannot construct an infinite large supercell, so we must make sure the supercell is large enough to prevent the defects in neighboring cells from interacting appreciably with each other. For this reason, a unit cell containing a few atoms is usually not appropriate for defect calculations. As for how large of the supercell is enough, convergence of the computed defect energy as a function of the supercell size can be checked. When the computed defect energy has converged, it can be assumed that defects in neighboring supercells no longer interact and the supercell is constructed large enough.

In this study, based on the optimized structural parameters for the perfect crystal CuO we obtained in Chapter 3, we constructed a supercell with $2 \times 3 \times 2$ times of a unit cell containing 96 atoms (Figure 4.1) for defect calculations. After the defect is introduced, the atoms in the supercell are allowed to relax. Numerical integrations over the first Brillouin zone were performed only at the Γ point because of the large size of supercells. This is also confirmed by performing the integrations with a $2 \times 2 \times 2$ k-point grid: the formation energies differences of a few typical defects are less than 0.1 eV between using only the Γ point and using the $2 \times 2 \times 2$ k-point grid. To check the convergence of the computed total energies, we also constructed a $2 \times 2 \times 2$ supercell containing 64 atoms. Compared to 96-atom supercells, the 64-atom supercells calculations yield very similar results, indicating convergence.

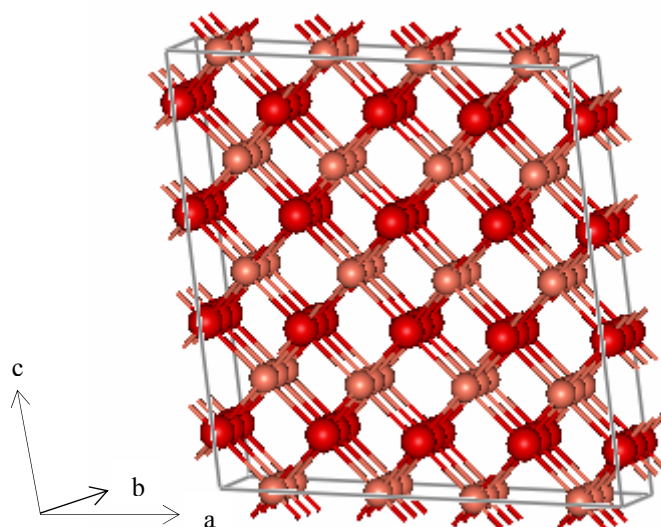


Figure 4.1 Structure of CuO supercell containing 96 atoms used in the study in this section. Black circles indicate O atoms, while grey circles indicate Cu atoms.

4.1.2 Calculating Formation Energies

Based on the standard formalism proposed by Zhang and Northrup [126], the formation energy H_f for an intrinsic defect with charge q (including its sign) in CuO can be expressed as

$$H_f = E_T(\text{defect}; q) - E_T(\text{perfect}) - n_{Cu}\mu_{Cu} - n_O\mu_O + qE_{VBM} + qE_F, \quad (4.1)$$

where $E_T(\text{defect}; q)$ and $E_T(\text{perfect})$ are the total energies of a supercell with the defect and the perfect supercell. n_{Cu} (n_O) denotes the number of copper (oxygen) atoms removed from (-) or added to (+) the perfect supercell and μ_{Cu} (μ_O) is the corresponding chemical potential. E_{VBM} is the energy of the valence-band maximum and E_F is the Fermi energy defined to be zero at the valence-band maximum with a maximum value equal to the energy band gap we obtained in Chapter 3, 1.0 eV.

From equation (4.1) we see that the formation energies of native point defects depend on the chemical potentials of Cu and O, and also vary with the Fermi energy. The chemical potentials of Cu and O depend on the experimental growth conditions, which can be Cu-rich or O-rich or anything in between. Under Cu-rich conditions, the copper is assumed in thermodynamic equilibrium with the bulk solid Cu and therefore $\mu_{Cu} = \mu_{Cu[\text{bulk}]}$, where $\mu_{Cu[\text{bulk}]}$ is the total energy per atom of metallic Cu. The O chemical potential in this case is not independent but constrained by the equilibrium condition

$$\mu_O + \mu_{Cu} = \mu_{CuO}. \quad (4.2)$$

Under O-rich conditions, the oxygen is assumed to be in equilibrium with O_2 gas, so its chemical potential is $\mu_{O[\text{gas}]}$, the total energy per atom of molecular O_2 . In this case, μ_{Cu} is then obtained from condition (4.2). To obtain $\mu_{Cu[\text{bulk}]}$ and $\mu_{O[\text{gas}]}$, separate calculations were performed to get the total energies of metallic Cu with fcc structure and molecular O_2 . For metallic Cu, a $16 \times 16 \times 16$ k-point set generated by the Monkhorst-Pack scheme [92] and the cutoff energy of 342 eV were used. The optimized lattice parameter was 3.52 Å, which is in good agreement with experimental

value of 3.61 Å [122]. In the case of O₂, only Γ point was used and an O₂ molecule placed in a cubic cell with the dimension of 16Å was allowed to relax. The optimized O-O bond length we obtained is 1.22 Å, very close to experimental value 1.21 Å [127]. Our calculated values of $\mu_{\text{Cu}[\text{bulk}]}$ and $\mu_{\text{O}[\text{gas}]}$ are -4.71 eV and -5.24 eV, respectively.

4.2 Results and Discussions

We have considered three different types of native point defects: vacancies (V_{Cu} , V_{O}), antisite defects (Cu_{O} , O_{Cu}) and isolated interstitials (Cu_{i} , O_{i}). A vacancy is introduced by removing a Cu atom or O atom from the supercell. For the antisite defects, an O atom is replaced by a Cu atom or a Cu atom is substituted by an O atom in the supercell. In the case of isolated interstitials, an atom of Cu or O is put on the possible sites in the supercell. In this study, the central “empty” position of the unit cell (see Figure 4.2) is considered as a possible interstitial site. For each defect species, we have considered its charge q neutral to fully ionized states: -2~0 for a Cu vacancy V_{Cu} , 0~+2 for an O vacancy V_{O} , 0~+2 for antisite Cu_{O} , -2~0 for antisite O_{Cu} , 0~+2 for a Cu interstitial Cu_{i} , and -2~0 for an O interstitial O_{i} .

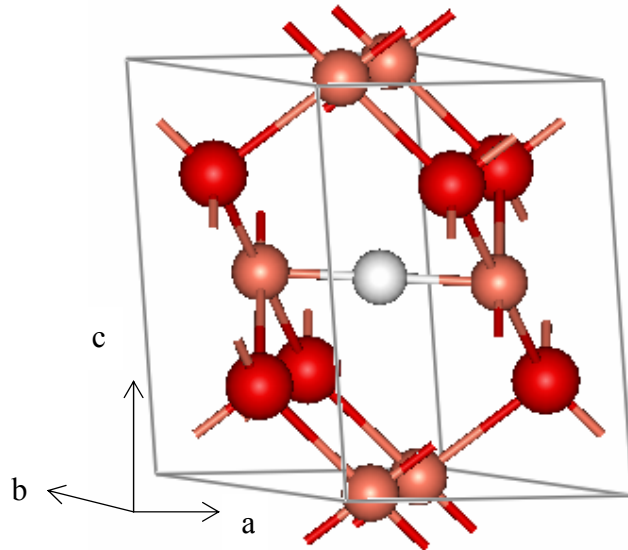


Figure 4.2 Initial interstitial position considered in the unit cell of CuO. Black circles indicate O atoms, while grey circles indicate Cu atoms. The interstitial is represented by a light grey circle.

4.2.1 Electronic Structures and Structural Relaxations

After a defect is introduced, structural relaxations take place around the defect. The distances between a defect and its neighboring atoms before and after the relaxations were examined and summarized in Table 4.1. Because of the low symmetry of the monoclinic structure, the atoms in a certain coordination shell do not always have equal distance from a defect. In this case, the average distance is listed in the table. For example, an O vacancy site has four Cu ions as first nearest neighbors (1st n.n.): two are 1.900 Å and another two are 1.906 Å from the defect site. So the average value 1.903 Å is listed in the table as the distance.

As seen from the table, in the presence of V_{Cu}^0 , while 1st n.n. O ions relaxed outward nearly 11%, 2nd n.n. O ions show very slightly inward relaxations and 2nd n.n. Cu ions also exhibit inward relaxations of about 2%. This can be explained in terms of ionic size and charge effects. When a Cu atom is removed to form the vacancy, 1st n.n. O ions are no longer electrostatically attracted to the vacancy and therefore move away from the vacancy. In contrast, 2nd n.n. Cu ions move closer to the vacancy because electrostatic repulsions of Cu-Cu are reduced by the introduced vacancy. When negative charge states of V_{Cu} increase, 2nd n.n. Cu ions continue to move toward the vacancy because of the electrostatic attraction between V_{Cu} and 2nd n.n. Cu ions. Compared to the 2nd n.n. Cu ions, the distances between V_{Cu} and 1st n.n. O ions do not change so much with increasing charge states of V_{Cu} . This is because O ions with a large ionic size are subject to significant electrostatic repulsions with surrounding O ions and therefore they are energetically more difficult to relax than Cu ions, even in the presence of the charged defects.

Table 4.1 Structural relaxations around native point defects. Average distances from the defect positions to neighboring ions are listed. Neighboring atomic species and their coordination number are also shown in parentheses.

	Distance in Å (atomic species; coordination number)	
	1 st n.n.	2 nd n.n.
Cu (bulk CuO)	1.903 (O;4)	2.713 (O;2), 2.822 (Cu;4)
V _{Cu} ⁰	2.112 (O;4)	2.709 (O;2), 2.763 (Cu;4)
V _{Cu} ¹⁻	2.116 (O;4)	2.702 (O;2), 2.757 (Cu;4)
V _{Cu} ²⁻	2.115 (O;4)	2.701 (O;2), 2.751 (Cu;4)
O _{Cu} ⁰	1.886 (O;4)	2.772 (Cu; 4)
O _{Cu} ¹⁻	2.076 (O;4)	2.695 (Cu;4)
O _{Cu} ²⁻	2.254 (O;4)	2.414 (Cu;4)
O (bulk CuO)	1.903 (Cu;4)	2.554 (O;2), 2.713 (Cu;2)
V _O ⁰	1.828 (Cu;4)	2.438 (O;2), 2.697 (Cu;2)
V _O ¹⁺	1.852 (Cu;4)	2.440 (O;2), 2.702 (Cu;2)
V _O ²⁺	1.888 (Cu;4)	2.442 (O;2), 2.704 (Cu;2)
Cu _O ⁰	2.190 (Cu;4)	2.437 (Cu;2), 2.545 (O;2)
Cu _O ¹⁺	2.228 (Cu;4)	2.369 (Cu;2), 2.436 (O;2)
Cu _O ²⁺	2.225 (Cu;4)	2.372 (Cu;2), 2.451 (O;2)
interstitial (bulk CuO)	1.411 (Cu;2)	1.872 (O;2)
Cu _i ⁰	1.780 (O;2)	2.247 (Cu;2)
Cu _i ¹⁺	1.893 (O;2)	2.128 (Cu;2)
Cu _i ²⁺	1.887 (O;2)	2.130 (Cu;2)
O _i ⁰	1.797 (Cu;2)	1.939 (O;2)
O _i ¹⁻	1.746 (Cu;2)	2.165 (O;2)
O _i ²⁻	1.723 (Cu;2)	2.252 (O;2)

In the case of V_O⁰, 1st n.n. Cu ions show inward relaxation of about 4%, and 2nd n.n. O ions and Cu ions also move toward the vacancy by 4.5% and 0.6%, respectively. Such inward relaxation of 1st n.n. Cu ions is contrary to the case of V_{Cu}⁰ and can be understood by noting the large ionic size of oxygen. When an O atom is removed, attractive interactions of the O atom and 1st n.n. Cu ions no longer exist, but an open space is formed by the vacancy. Because of this open space by the V_O formation, 1st n.n. Cu ions with a small ionic size can move closer to the vacancy site. 2nd n.n. O ions have a bigger percentage inward relaxation because the repulsive interactions of the O ions

and the O atom have disappeared due to the formation of the vacancy. When the charge of the vacancy increases, 1st n.n. Cu ions relax slightly away from the vacancy compared to the case of the neutral state of the vacancy because of the electrostatic repulsions between 1st n.n. Cu ions and V_O with a positive charge.

When an O atom is replaced by a Cu atom (antisite Cu_O), 1st n.n. Cu ions surrounding the original O atom relaxed outwardly more than 15%. This is reasonable because Cu ions will repel each other after the disappearance of the attractive forces between 1st n.n. Cu ions and the O atom. With increasing charge of the antisite, 1st n.n. Cu ions move further away from the antisite. For the antisite O_{Cu}, 1st n.n. O ions move toward the neutral antisite slightly because of the space cleared by the large-size Cu atom. For charged antisite O_{Cu}, however, 1st n.n. O ions move away from the charged antisite by more than 9%. This can be attributed to the repulsions between 1st n.n. ions and the negative charged antisite.

The interstitial site has two 1st n.n. Cu ions at 1.411 Å and two 2nd n.n. O ions at 1.872 Å. In the presence of Cu_i⁰, Cu ions surrounding this interstitial exhibit a huge outward relaxation of more than 59%, while O ions show inward relaxation of about 5%. Because of the relaxations, two O ions became 1st n.n. ions located at 1.780 Å and two Cu ions became 2nd n.n. ions located at 2.247 Å. As the charge of the interstitial increases, the two O ions move away from Cu_i and the distances between them are very close to Cu-O bond lengths in perfect CuO (1.900 and 1.906 Å) while two Cu ions move closer to Cu_i. In the case of O_i⁰, 1st n.n. Cu ions also show outward relaxation of about 27%, much less than that in the case of Cu_i⁰. The relaxed distances between Cu ions and O_i⁰ (1.797 Å) are close to Cu-O bond lengths in perfect CuO. 2nd n.n. O ions move away from O_i⁰ as well in this case. When the negative charge of the O interstitial increases, Cu ions move closer to the interstitial while O ions move farther away from the interstitial due to the electrostatic interactions between the ions and the charged interstitial.

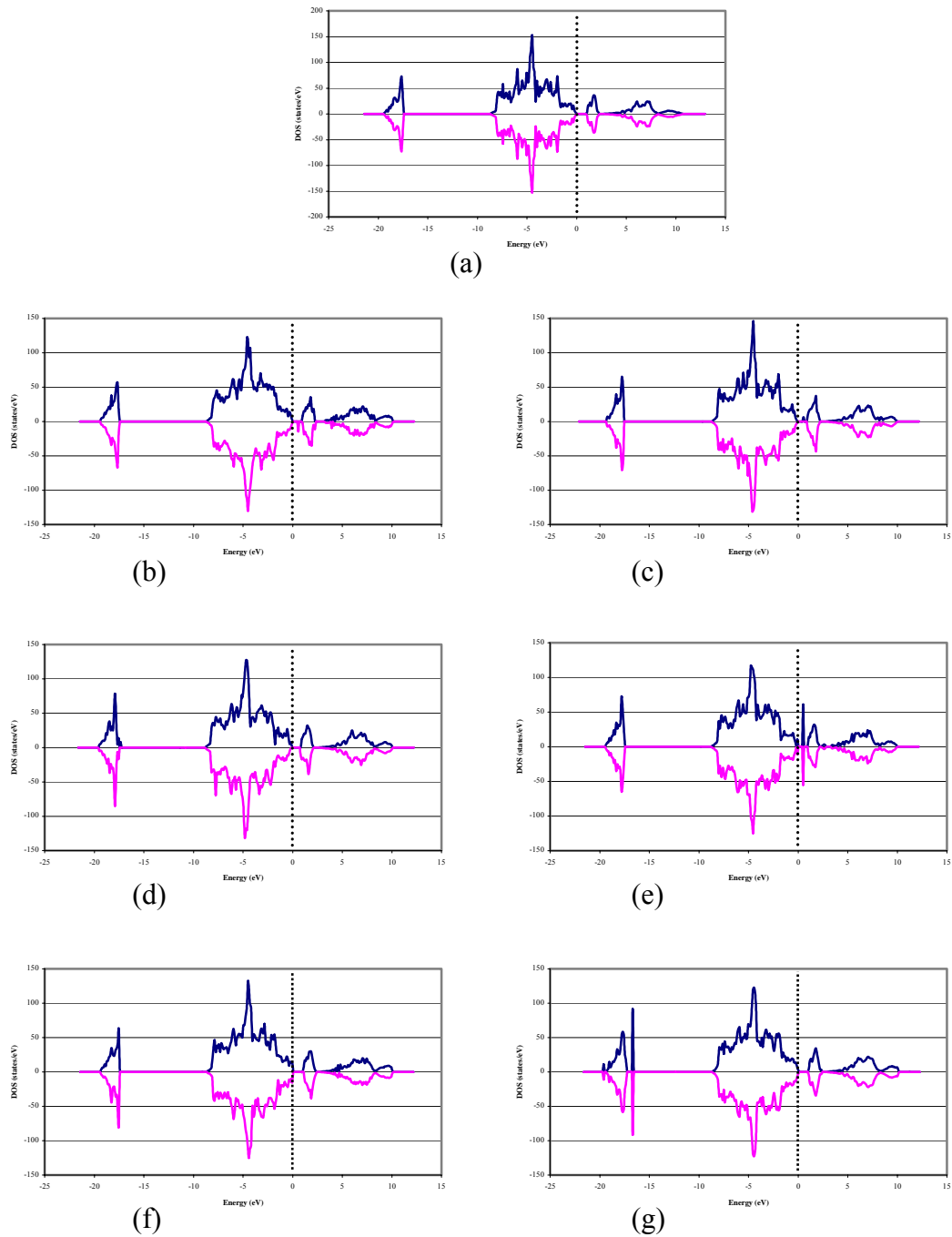


Figure 4.3 Densities of states (DOS) for perfect CuO supercell and defective supercells. The valence band maxima are set at 0 eV. The majority is plotted upward; while the minority is plotted downward. (a) Perfect, (b) CuO^0 , (c) O_{Cu}^0 , (d) V_{Cu}^0 , (e) V_{O}^0 , (f) Cu_i^0 , and (g) V_i^0 .

Native point defects not only cause structure relaxations around the defect in CuO, but also lead to changes to the electronic structures of the crystal by inducing defect levels. Calculated densities of states (DOS) with k -point density of $4 \times 4 \times 4$ for the perfect supercell and those containing six kinds of neutral native point defects are shown in Figure 4.3. In this figure, the valence band maxima are set at 0 eV.

From Figures 4.3 (a)-(g), we see that extra levels can be observed in the density of states in defective configurations although the overall DOS profiles for these defective supercells are similar to that of perfect CuO supercell. In the case of Cu_O^0 , a deep level is present at about 0.56 eV in the band gap. This state is occupied by an electron with down spin. O_Cu^0 also induces a deep level at about 0.53 eV but occupied by an electron with up spin. In the case of V_Cu^0 , two extra levels appear in the low-energy valence band. For V_O^0 , an unoccupied extra level is introduced in the center of the band gap. In the case of Cu_i^0 , no apparent defect levels can be observed from the graph but the majority DOS and the minority DOS are no longer symmetric because of the defect. For O_i^0 , like V_Cu^0 , two extra levels are present in the low-energy valence band.

4.2.2 Formation Energies

As stated earlier, formation energies depend not only on atomic chemical potentials but also on the Fermi level. In Figure 4.4 and Figure 4.5, we show our calculated formation energies H_f for native point defects in CuO as a function of the Fermi level E_F , in the O-rich and Cu-rich limits, respectively. For each defect species, only the lowest-energy charge states with respect to E_F are shown in the figures. We see that our results in these two extreme cases are very similar. This is because the calculated chemical potentials of Cu in bulk solid copper and O in O_2 gas are close. While the stable charge states of some defect species are varying with the position of the Fermi level, some defects have only one stable charge state in the whole range of the Fermi level. For example, V_Cu^{2-} is always the most stable defect in copper vacancies. It can be seen that when E_F is close to E_{VBM} (0 eV), the stable charge states for each defect are Cu_O^{2+} , Cu_i^0 , V_O^0 , O_i^0 , O_Cu^{2-} , V_Cu^{2-} . On the other hand, when E_F is

close to E_{CBM} (1.0 eV), Cu_O^0 , Cu_i^0 , V_O^0 , O_i^{2-} , O_Cu^{2-} , V_Cu^{2-} are the most stable defects.

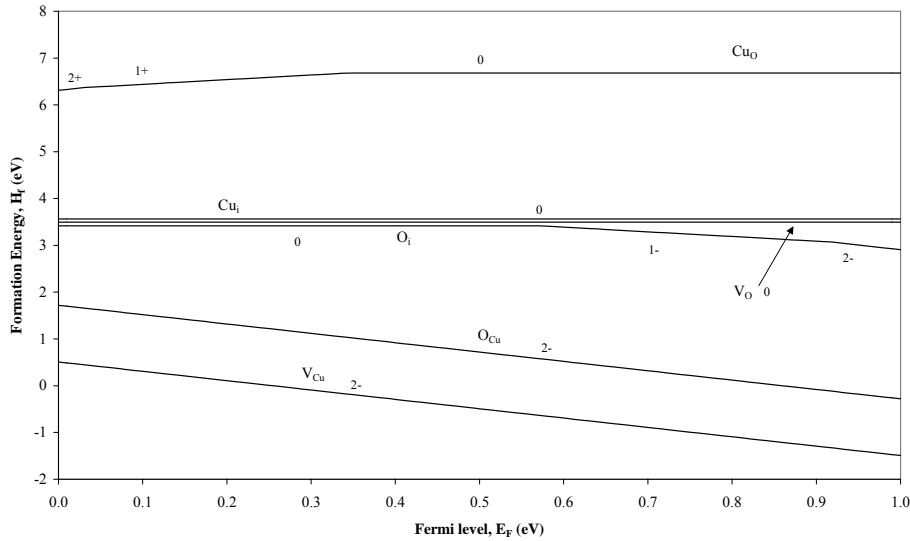


Figure 4.4 Formation energies of native point defects in CuO as a function of the Fermi level E_F in the O-rich environment. For each defect species, only the lowest-energy charge states with respect to E_F are shown. The zero energy of E_F corresponds to the valance band maximum.

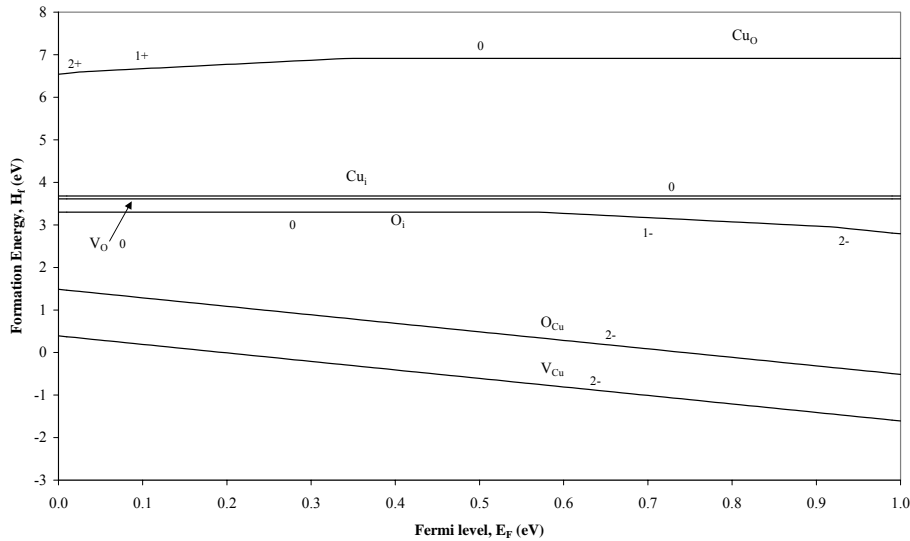


Figure 4.5 Formation energies of native point defects in CuO as a function of the Fermi level E_F in the Cu-rich environment. For each defect species, only the lowest-energy charge states with respect to E_F are shown. The zero energy of E_F corresponds to the valance band maximum.

An important conclusion we can draw from these two figures is that in both the O-rich and the Cu-rich environments, V_{Cu}^{2-} always has the lowest formation energy (less than 1.0 eV), indicating that this defect is very easy to form during the growth of crystal CuO. This means that intrinsically, CuO is a *p*-type semiconductor. They will act as a sink for any excess of electrons in the material. This result is in agreement with many experiments [8, 18-20].

CHAPTER 5

CONCLUSION AND FURTHER WORK

In this thesis, we have performed the first-principles study on the strongly correlated cupric oxide (CuO), both perfect and with various native point defects. The LSDA+U method implemented with the PAW potentials were used in the calculations. The optimized structural parameters obtained agree very well with experimental values, suggesting the validities of the LSDA+U method and the PAW potentials we used.

Using the optimized structural parameters, we have studied the ground state electronic and magnetic properties of CuO. As a comparison, the electronic structure was also studied by the LSDA method. Our results from the electronic structure obtained by the LSDA+U method showed that CuO is a semiconductor with an indirect gap of about 1.0 eV, which is consistent with experimental results. By calculating and comparing the total energies with all possible spin directions of the four Cu atoms in the unit cell, we found an antiferromagnetic ground state for CuO, which has been confirmed by many experiments. Another important conclusion from these calculations is that while the LSDA approximation predicts CuO incorrectly with a non-magnetic and metallic ground state, the LSDA+U method showed it to be antiferromagnetic and

semiconducting. This suggests that the LSDA+U method indeed makes significant improvements over the LSDA method for the strongly correlated systems.

To calculate the formation energies of various native point defects, the unit cell of CuO was expanded into a supercell containing 96 atoms in the perfect crystal case. According to our results, copper vacancies are the most stable defects in CuO, both in Cu-rich and in O-rich environments. Among the copper vacancies, the charge state V_{Cu}^{2-} exhibits a negative formation energy value, indicating that this point defect is easy to form at even low temperatures. Therefore, CuO is intrinsically a p-type semiconductor, which also agrees with several experiments.

Our main goal in this research is to investigate CuO as a potential material to produce low-cost large-scale solar cells. Since the fabrication of both p-type and n-type doped layers to form the p-n junction is required in virtually all electronic and optoelectronic devices, our further work shall be concentrated on the doping effects on CuO by introducing some impurities such as Ni, Zn etc. Special focus should be put on the n-type doping because of its intrinsic p-type nature as we discussed.

REFERENCES

- [1] G. R. Davis, *Scientific American* **263**, 21-27, (1990).
- [2] R. A. Messenger and J. Ventre, *Photovoltaic Systems Engineering, Second Edition*, CRC Press, 2004, p. 21.
- [3] J. Nijs, *Int. J. Solar Energy* **15**, 91-122 (1994).
- [4] W. Wang, O. K. Varghese, C. Ruan, M. Paulose, and C. A. Grimes, *J. Mater. Res.*, **18**, 2756 (2003).
- [5] J. Ghijsen, L. H. Tjeng, J. van Elp, H. Eskes, J. Westerink, G. A. Sawatzky, and M. T. Czyzyk, *Phys. Rev. B* **38**, 11322 (1988).
- [6] Y. S. Chaudhary, A. Agrawal, R. Shrivastav, V. R. Satsangi, and S. Dass, *International Journal of Hydrogen Energy* **29**, 131-134 (2004).
- [7] F. Marabelli, G. B. Parravicini, and F. Salghetti-Drioli, *Phys. Rev. B* **52**, 1433 (1995).
- [8] S. C. Ray, *Solar energy materials & solar cells* **68**, 307-312 (2001).
- [15] U. D. Lanke and M. Vedawyas, *Nucl. Inst. Meth. Phys. Res. B* **155**, 97 (1999).
- [16] T. Maruyama, *Solar energy materials & solar cells* **56**, 85 (1998).
- [11] P. Poizot, S. Laruelle, S. Grugeon, L. Dupont, and J-M. Tarascon, *Nature* **407**, 496 (2000).
- [12] R. V. Kumar, Y. Diamant, and A. Gedanken, *Chem. Mater.* **12**, 2301 (2000).
- [13] R. Ao, L. Kummerl, and D. Haarer, *Adv. Mater.* **7**, 495 (1995).

- [14] M. Singhai, V. Chhabra, P. Kang, and D. O. Shah, *Mater. Res. Bull.* **32**, 239 (1997).
- [15] Y. Jiang, S. Decker, C. Mohs, and K. J. Klabunde, *J. Catal.* **180**, 24 (1998).
- [16] T. Ishihara, M. Higuchi, T. Takagi, M. Ito, H. Nishiguchi, and Y. Takita, *J. Mater. Chem.* **8**, 2037 (1998).
- [17] S. Åsbrink and L.-J. Norrby, *Acta Cryst. B* **26**, 8 (1970).
- [18] K.L. Hardee and A.J. Bard, *J. Electrochem. Soc.* **124**, 215 (1977).
- [19] F.P. Koffyberg and F.A. Benko, *J. Appl. Phys.* **53**, 1173 (1982).
- [20] F. Marabelli, G.B. Parravicini, and F. Salghetti-Drioli, *Phys. Rev. B* **52**, 1433 (1995).
- [21] J.B. Forsyth, P.J. Brown, and B.M. Wanklyn, *J. Phys. C* **21**, 2917 (1988).
- [22] B.X. Yang, J.M. Tranguada, and G. Shirane, *Phys. Rev. B* **38**, 174 (1988).
- [23] B.X. Yang, T.R. Thurston, J.M. Tranquada, and G. Shirane, *Phys. Rev. B* **39**, 4343 (1989).
- [24] P.J. Brown, T. Chattopadhyay, J.B. Forsyth, V. Nunez, and F. Tasset, *J. Phys.: Condens. Matter* **3**, 4281 (1991).
- [25] M. Ain, A. Menelle, B.M. Wanklyn, and E.F. Bertaut, *J. Phys.: Condens. Matter* **4**, 5327 (1992).
- [26] J. Ghijsen, L.H. Tjeng, J. van Elp, H. Eskes, J. Westerink, G.A. Sawatzky, and M.T. Czyzyk, *Phys. Rev. B* **38**, 11322 (1988).
- [27] K. Terakura, T. Oguchi, A.R. Williams, and J. Kubler, *Phys. Rev. B* **30**, 4734 (1984)

- [28] G. Grioni, M.T. Czyzyk, F.M.F de Groot, J.C.Fuggle, and B.E. Watts, Phys. Rev. B **39**, 4886 (1989).
- [29] W.Y. Ching, Y.-N. Xu, and K.W. Wong, Phys. Rev. B **40**, 7684 (1989).
- [30] P. Hohenberg and W.Khon, Phys. Rev. **136**, B864 (1964).
- [31] W. Kohn and L. J. Sham, Phys. Rev. **140**, A1133 (1965).
- [32] U. von Barth and L. Hedin, J. Phys. C: Solid State Phys. **5**, 1629 (1972).
- [33] O. Gunnarsson and B. I .Lundqvist, Phys. Rev. **13**, 4274 (1976).
- [34] S. H. Vosko, L. Wilk, and M. Nusair, Can. J. Phys. **58**, 1200 (1980).
- [35] J.P. Perdew and A. Zunger, Phys. Rev. B **23**, 5048 (1981).
- [36] J.P. Perdew, R. G. Parr, M. Levy and J. L. Balduz, Jr., Phys. Rev. Lett **49**, 1691 (1982).
- [37] V. I. Anisimov, J. Zaanen, and O. K. Andersen, Phys. Rev. B **44**, 943 (1991).
- [38] P. Raybaud, G. Kresse, J. Hafner and H. Toulhoat, J. Phys.: Condens. Matter **9**, 11085 (1997).
- [39] J. P. Perdew and Y. Wang, Phys. Rev. B **33**, 8800 (1986).
- [40] J. P. Perdew in *Electronic Structure of Solids*, edited by Ziesche and H. Eschrig Akademie Verlag, Berlin, 1991.
- [41] J. P. Perdew and Y. Wang, Phys. Rev. B **45**, 13244 (1992).
- [42] J. P. Perdew and K. Burke, Int. J. Quantum Chem. **57**, 309 (1996).
- [43] J. P. Perdew, K. Burke, and Y. Wang, Phys. Rev. B **54**, 16533 (1996).
- [44] J. P. Perdew, K. Burke, and M. Ernzerhof, Phys. Rev. Lett. **77**, 3865 (1996).
- [45] S. Kurth, J. P. Perdew and P. Blaha, Int. J. Quantum. Chem. **75**, 889 (1999).

- [46] C. Adamo, M. Ernzerhof and G. E. Scuseria, *J. Chem. Phys.* **112**, 2643 (2000).
- [47] A. Svane and O. Gunnarsson, *Phys. Rev. Lett.* **65**, 1148 (1990).
- [48] L. Hedin, *Phys. Rev.* **139**, A796 (1965).
- [49] L. Hedin and S. Lundqvist, in *Solid State Physics Vol 23*, Edited by H. Ehrenreich, F. Seitz and D. Turnbull, Academic, New York, 1969, p. 1.
- [50] F. Aryasetiawan, *Phys. Rev. B* **46**, 13051 (1992).
- [51] F. Aryasetiawan and O. Gunnarsson, *Phys. Rev. Lett.* **74**, 3221 (1995).
- [52] V. I. Anisimov, M. A. Korotin, J. Zaanen, and O.K. Andersen, *Phys. Rev. Lett.* **68**, 343 (1992).
- [53] V. I. Anisimov, I. V. Solovyev, M. A. Korotin, M. T. Czyzyk, and G. A. Sawatzky, *Phys. Rev. B* **48**, 16929 (1993).
- [54] V. I. Anisimov, P. Kuiper, and J. Nordgren, *Phys. Rev. B* **50**, 8257 (1994).
- [55] M.T.Czyzyk and G.A.Sawatzky, *Phys. Rev. B* **49**, 14211 (1994).
- [56] I. V. Solovyev, P. H. Dederichs, and V. I. Anisimov, *Phys. Rev. B* **50**, 16861 (1994).
- [57] A.I. Liechtenstein, V.I. Anisimov, and J. Zaanen, *Phys. Rev. B* **52**, R5467 (1995).
- [58] V.I. Anisimov, F. Aryasetiawan, and A.I. Liechtenstein, *J. Phys.: Condens. Matter* **9**, 767 (1997).
- [59] S. L. Dudarev, A.I. Liechtenstein, M. R. Castell, G. A. D. Briggs, and A. P. Sutton, *Phys. Rev. B* **56**, 4900 (1997).
- [60] S. L. Dudarev, G. A. Botton, S. Y. Savrasov, C. J. Humphreys, and A. P. Sutton, *Phys. Rev. B* **57**, 1505 (1997).

- [61] W.E. Pickett, S.C. Erwin, and E.C. Ethridge, *Phys. Rev. B* **58**, 1201 (1998).
- [62] J. Hubbard, *Proc. R. Soc. London, Ser. A* **276**, 238 (1963).
- [63] M. Born and J. R. Oppenheimer, *Ann. Physik* **84**, 457 (1927).
- [64] M. Born and K. Huang, *Dynamical Theory of Crystal Lattices*, Oxford University Press, Oxford, 1954.
- [65] M. Levy, *Proc. Nat. Acad. Sci. USA* **76**, 6062 (1979).
- [66] M. Levy, *Phys. Rev. A* **26**, 1200 (1982).
- [67] M. Levy and J. P. Perdew, in *Density Functional Methods in Physics*, edited by R. M. Dreizler and J. da Providencia, Plenum, New York, 1985, p. 11.
- [68] E. Lieb, in *Physics as Natural Philosophy*, edited by A. Shimony and H. Feshback, MIT Press, Cambridge, 1982, p. 111.
- [69] E. Lieb, *Int. J. Quant. Chem.* **24**, 243 (1983).
- [70] E. Lieb, in *Density Functional Methods in Physics*, edited by R. M. Dreizler and J. da Providencia, Plenum, New York, 1985, p. 31.
- [71] J. Cho and M. Scheffler, *Phys. Rev. B* **53**, 10685 (1996).
- [72] D. J. Singh, W. E. Pickett, and H. Krakauer, *Phys. Rev. B* **43**, 11628 (1991).
- [73] T. C. Leung, C. T. Chan, and B. N. Harmon, *Phys. Rev. B* **44**, 2923 (1991).
- [74] J. Zhu, X. W. Wang, and S. G. Louie, *Phys. Rev. B* **45**, 8887 (1992).
- [75] M. Körling and J. Häglund, *Phys. Rev. B* **45**, 13293 (1992).
- [76] K. Terakura, T. Oguchi, A. R. Williams, and J. Kübler, *Phys. Rev. Lett.* **52**, 1830 (1984); *Phys. Rev. B* **30**, 4734 (1984).
- [77] G. A. Sawatzky and J. W. Allen, *Phys. Rev. Lett.* **53**, 2239 (1984).

- [78] J. Zaanen, O. Jepsen, O. Gunnarsson, A. T. Paxton, O. K. Andersen, and A. Svane, *Physica C* **153-155**, 1636 (1988).
- [79] P. Dufek, P. Blaha, V. Sliwko, and K. Schwarz, *Phys. Rev. B* **49**, 10170 (1994).
- [80] D. R. Hartree, *Proc. Cambridge Philos. Soc.* **24**, 89 (1928).
- [81] V. Fock, *Z. Phys.* **61**, 126 (1930).
- [82] J. C. Slater, *Phys. Rev.* **35**, 210 (1930).
- [83] S. Massida, M. Posternak, and A. Baldereschi, *Phys. Rev. B* **48**, 5058 (1993).
- [84] P. W. Anderson, *Phys. Rev* **124**, 41 (1961).
- [85] D. A. Zatsépin, V. R. Galakhov, M. A. Korotin, V. V. Fedorenko, E. Z. Kurmaev, S. Bartkowski, M. Neumann, and R. Berger, *Phys. Rev. B* **57**, 4377 (1998).
- [86] O. Bengone, M. Alouani, P. E. Blöchl, and J. Hugel, *Phys. Rev. B* **62**, 16392 (2000).
- [87] A. Rohrbach, J. Hafner, and G. Kresse, *J. Phys.: Condens. Matter* **15**, 979 (2003).
- [88] F. Bloch, *Z. Phys.* **52**, 555 (1928).
- [89] N. W. Ashcroft and N. D. Mermin, *Solid State Physics*, Holt Saunders, Philadelphia. 1976.
- [90] A. Baldereschi, *Phys. Rev. B* **7**, 5212 (1973).
- [91] D. J. Chadi and M. L. Cohen, *Phys. Rev. B* **8**, 5747 (1973).
- [92] H. J. Monkhorst and J. D. Pack, *Phys. Rev. B* **13**, 5188 (1976). *Phys. Rev. B* **16**, 1748 (1977).
- [93] W. E. Pickett, *Comput. Phys. Rep.* **9**, 115 (1989).
- [94] J. C. Phillips, *Phys. Rev.* **112**, 685 (1958).

- [95] J. C. Phillips and L. Kleinman, *Phys. Rev.* **116**, 287 (1959).
- [96] W. A. Harrison, *Pseudopotentials in the Theory of Metals*, Benjamin, New York, 1966.
- [97] V. Heine, in *Solid State Physics*, edited by H. Ehrenreich, F. Seitz, and D. Turnbull, Academic, New York, 1970, p. 1.
- [98] M. L. Cohen and V. Heine, in *Solid State Physics*, edited by H. Ehrenreich, F. Seitz, and D. Turnbull, Academic, New York, 1970, p. 37.
- [99] M. T. Yin and M. L. Cohen, *Phys. Rev. B* **25**, 7403 (1982).
- [100] P. E. Blöchl, *Phys. Rev. B* **41**, 5414 (1990).
- [101] D. Vanderbilt, *Phys. Rev. B* **41**, 7892 (1990).
- [102] K. Laasonen, A. Pasquarello, R. Car, C. Lee, and D. Vanderbilt, *Phys. Rev. B* **47**, 10142 (1993).
- [103] G. Kresse and J. Hafner, *Phys. Rev. B* **48**, 13115 (1993).
- [104] G. Kresse and J. Hafner, *J. Phys.: Condens. Matter* **6**, 8245 (1994).
- [105] J. Yamauchi, M. Tsukada, S. Watanabe, and O. Sugino, *Phys. Rev. B* **54**, 5586 (1996).
- [106] A. Dal Corso, A. Pasquarello, and A. Baldereschi, *Phys. Rev. B* **56**, R11369 (1997).
- [107] G. Kresse and D. Joubert, *Phys. Rev. B* **59**, 1758 (1999).
- [108] P. E. Blöchl, *Phys. Rev. B* **50**, 17953 (1994).
- [109] N. A. W. Holzwarth, G. E. Matthews, R. B. Dunning, A. R. Tackett, and Y. Zeng, *Phys. Rev. B* **55**, 2005 (1997).

- [110] H. Krakauer, M. Posternak, and A. J. Freeman, *Phys. Rev. B* **19**, 1706 (1979).
- [111] E. Wimmer, H. Krakauer, M. Weinert, and A. J. Freeman, *Phys. Rev. B* **24**, 864 (1981).
- [112] L. F. Mattheiss and D. R. Hamann, *Phys. Rev. B* **33**, 823 (1986).
- [113] P. Blaha, K. Schwarz, P. Sorantin, and S. B. Trickey, *Computer Phys. Commun.* **59**,399 (1990).
- [114] G. Kresse and J. Hafner, *Phys. Rev. B* **47**, 558 (1993).
- [115] G. Kresse and J. Hafner, *Phys. Rev. B* **49**, 14251 (1994).
- [116] G. Kresse and J. Furthmüller, *Phys. Rev. B* **54**, 11169 (1996).
- [117] G. Kresse and J. Furthmüller, *Comput. Mater. Sci.* **6**, 15 (1996).
- [118] D. M. Ceperley and B. J. Alder, *Phys. Rev. Lett.* **45**, 566 (1980).
- [119] O. Gunnarsson, O. K. Andersen, O. Jepsen, and J. Zaanen, *Phys. Rev. B* **39**, 1708 (1989).
- [120] G. T. Tunell, E. Posnjak, and C. J. Ksanda, *Z. Kristallogr.* **90A**, 120 (1935).
- [121] H. E. Swanson, E. Tatge, and R. K. Fuyat, *Standard X-ray Diffraction Powder Pattern*, Natl. Bur. Stand.(U.S.) Circ. No. 539, U.S. GPO, Washington, DC, 1953, p. 1.
- [122] R. W. G. Wyckoff, *Crystal Structures*, Interscience Publishers, New York, 1963, p. 140.
- [123] C.J. Bradley, *The Mathematical Theory of Symmetry in Solids: Representation Theory for Point Groups and Space Groups*, Clarendon Press, Oxford, 1972, p. 96.
- [124] B. N. Brockhouse, *Phys. Rev.* **94**, 781 (1954).

- [125] M. Takahashi and J. Igarashi, *Phys. Rev. B* **56**, 12818 (1997).
- [126] S. B. Zhang and J. E. Northrup, *Phys. Rev. Lett.* **67**, 2339 (1991).
- [127] A. A. Radzig and B. M. Smirnov, *Reference Data on Atoms, Molecules, and Ions*, Springer-Verlag, Berlin Heidelberg, 1985, p. 350.
- [128] R. M. Martin, *Electronic Structure: Basic Theory and Practical Methods*, Cambridge University Press, Cambridge, UK, 2004.

BIOGRAPHICAL INFORMATION

Dangxin Wu received his Bachelor degree in Materials Science from Sichuan University in 1998. He received his Master of Science degree in Physics from the University of Texas at Arlington in August 2005.